Research and Application of Materials Science

Publisher: Viser Technology Pte. Ltd.

ISSN: 2661-4464(online)
2661-4456(print)

Frequency: Semi-annual

Add.: 195 Pearl's Hill Terrace, #02-41,
Singapore 168976

https://www.viserdata.com/

Research and Application of Materials Science

Volume 7 No.1 (2025)

CONTENTS

Viser Technology Pte. Ltd.
Research and Application of Materials Science
DOI: 10.33142/rams.v7i1.18639

Research Article Open Access

High Performance N, C -Codoped $Na_3V_2(PO_4)_3$ Cathode Material for Sodium-ion Batteries

Jiayu LI*, Xiao FU

Public Experiment Center, University of Shanghai for Science and Technology, Shanghai, 200093, China

*Corresponding Author: Jiayu Li, E-mail: 249595941@qq.com

Abstract

A typical NASICON type cathode material, $Na_3V_2(PO_4)_3$ (NVP) has been widely studied in the field of sodium-ion batteries (SIBs), which possesses a suitable price, an ideal specific capacity, and an excellent cycling stability. However, its low ionic/electronic conductivity has become a major factor hindering its development. In the present study, carbon and nitrogen co-doped NVP (NVP/CN) composites are synthesized by adding $C_3N_6H_6$ source using a simple preparation method. The carbon and nitrogen co-doping is intended to introduce lattice defects, which enhances the electrical conductivity of the material and facilitates the diffusion of Na^+ and e^-. Comprehensively, the co-coated NVP cathode material show more excellent electrochemical performance when the N source addition of $nC_3N_6H_6$: nNVP=2 (NVP/CN-2). NVP/CN-2 has an initial discharge specific capacity of 111.5 mAh/g, and a capacity retention rate of 97.57% after 1000 charge/discharge cycles. The diffusion coefficient of sodium ions is relatively high and can reach 4.74×10-10 cm^2 s^{-1} by CV fitting, so the modified NVP/CN samples are expected to be promising cathode materials for sodium-ion batteries.

Keywords: *$Na_3V_2(PO_4)_3$; Modification; Sodium ion; Carbon-Nitrogen Co-Coating*

1 Introduction

Lithium-ion batteries, known for their high energy density, extended cycle life, and long-term usability, are currently widely applied in various fields such as portable power sources, electric vehicles, household appliances, smart wearable devices, and 3C products. They are also increasingly becoming the primary power source for new energy vehicles and energy storage, garnering significant attention in recent years[1-3]. However, as these Lithium-ion batteries are being utilized on a larger scale, cost and safety concerns are gaining prominence. Sodium-ion batteries (SIBs) hold promise as an alternative to lithium-ion batteries due to their cost-effectiveness and superior performance in high-low temperature environments [4-6]. Key factors determining the performance of sodium-ion battery cathode materials include the appropriate operating voltage, high reversible capacity, and structural stability[7]. A wide range of sodium-ion battery cathode materials have been reported, including layered and tunnel-type transition metal oxides, transition metal sulfides and fluorides, oxygen-containing anion compounds, Prussian blue analogs, and polymers[8-10]. However, due to the larger ionic radius of Na (1.02 Å) compared to Li (0.76 Å)[11], the sodium ion extraction process has implications for the stability, transport properties, and phase interconversion of material, resulting in suboptimal electrochemical performance[12-13].

Currently, cathode materials for sodium-ion batteries with the Na superionic conductor (NASICON) structure have garnered widespread attention[14-16]. These materials exhibit a three-dimensional open framework and larger interstitial channels, providing a theoretical basis for achieving rapid Na^+ transport[17-18]. One such material is NVP, which consists of VO_6 octahedral and PO_4 tetrahedral units. Sodium atoms reside in two distinct interstitial spaces and channels within the framework, creating two different oxygen environments[19]. This vanadium-based electrode exhibits two oxidation-reduction potentials at 3.4 V and 1.6 V, corresponding to the redox transitions of V^{3+}/V^{4+} and V^{2+}/V^{3+}. Notably, the 3.4 V flat plateau voltage is associated with a high theoretical capacity (117 mAh/g)[20]. To prevent the generation of V^{2+} during charge and discharge processes, voltage control is commonly employed to regulate electrochemical reactions, ensuring the reversibility of vanadium[21]. However, the intrinsic low electron conductivity of the material impacts its rate capability and cycling stability, mainly due to the relatively large atomic distances resulting from the independent VO_6 octahedral and PO_4 tetrahedral units that

Received on March 20, 2025; Accepted on April 30, 2025

make up the NASICON-type framework[22].

Thus, to address the aforementioned challenges and enhance the cycling performance and rate capability of $Na_3V_2(PO_4)_3$ batteries, two primary strategies have emerged. The first involves improving the material's interfacial performance. This can be achieved through carbon coating to enhance surface conductivity, resulting in a reduction in surface resistance[23-25]. Additionally, the introduction of metal ions to generate electrons or vacancies can enhance conductivity[26-27]. The second strategy centers on controlling the diffusion distance of sodium ions within the material. This is accomplished by reducing particle size and fabricating specialized positive electrode materials with features like porosity or mesoporosity, effectively shortening the migration pathway and enabling rapid charge and discharge in the battery[28-29].

In this study, we employ a straightforward hydrothermal assisted sol-gel approach to synthesize $Na_3V_2(PO_4)_3$/C cathode materials. By means of surface carbon and nitrogen co-coating modification, it is intended to effectively improve the electrical conductivity of $Na_3V_2(PO_4)_3$ cathode materials. Additionally, we utilize NaOH, NH_4VO_3, and $NH_4H_2PO_4$ as raw materials, with ascorbic acid as a reducing agent and $C_3N_6H_6$ as a nitrogen source. By adjusting the quantity of $C_3N_6H_6$ added, we examine its multifaceted impact on the structure, morphology, and electrochemical performance of the composite material. The experiments reveale that when the $C_3N_6H_6$: NVP ratio is 2 (molar ratio, n:n), the material exhibited the better outstanding performance.

2 Experimental Section

2.1 Materials synthesis

$Na_3V_2(PO_4)_3$/CN composites were prepared by a previously reported hydrothermal route combined with a sol-gel method[30-31]. In a typical synthesis process, the measured $NH_3H_2PO_4$ was meticulously dissolved in a NaOH solution, resulting in solution A. Concurrently, NH_4VO_3 was dissolved in an ascorbic acid solution, creating solution B. A was then gently introduced into B, magnetic stirring at room temperature to ensure adequate mixing, after which the mixture was transferred to a 40 ml Teflon-lined autoclave, the solution was heated at 190 ℃ in a closed autoclave and kept for 36 hours, then cooling naturally to room temperature. The resulting brown mixture was ultrasonicated for 120 minutes to homogenize the dispersion. upon cooling to room temperature, the gel was subjected to additional heating and stirring in a constant-temperature water bath at 75 ℃. Following these steps, the gel was dried in a 60 ℃ oven under atmospheric conditions for 12 hours. Subsequently, the milled powder underwent further heat treatment in a nitrogen atmosphere at 350 ℃ for 4 hours, followed by an 8-hour calcination at 800 ℃, cooled to room temperature and then grounded again to obtain the final product $Na_3V_2(PO_4)_3$/CN-x, abbreviated as NVP/CN-x. The prepared NVP/CN-x was based on the ratios of the amount of $C_3N_6H_6$ added, n_{C3N6H6}: n_{NVP} = 1, 2, 3, 4 named NVP/CN-1, NVP/CN-2, NVP/CN-3, and NVP/CN-4, respectively. For comparison, NVP/C prepared by the same method without $C_3N_6H_6$ addition of raw material was the comparative sample.

2.2 Material characterizations and electrochemical measurements

The crystal structures of all samples were determined using X-ray diffraction (XRD, Rigaku, Japan) in the scanning range of 10 °～60 ° at a scanning speed of 4 °/min. Surface morphology of the electrode materials was analyzed by scanning electron microscopy (SEM, ZEISS, SUPRA-55). Electrochemical characterization of $Na_3V_2(PO_4)_3$ electrodes were investigated by a coin half-cell (CR2032) assembled in an argon glove box. A working electrode was made by doping 80 wt% of active material (NVP, cathode electrode material), 10 wt% of acetylene black (conductive agent) and 10 wt% of polyvinylidene difluoride binder (PVDF) into N-methyl-2-pyrrolidone (NMP). The resulting paste was pasted onto aluminium foil, then the final cathode electrode sheet was obtained by drying the electrodes in a vacuum at 120 ℃ for 8 h. The electrolyte consisted of ethylene carbonate (EC), dimethyl carbonate (DEC) and fluoroethylene carbonate (FEC) in 1 M $NaClO_4$, where the volume ratio of EC to DEC was 1:1 and FEC was 5 wt%. Glass fiber membrane (Whatman, GF/D) was used as the septum and sodium foil as the anode electrode. The charge/discharge performance was tested at room temperature (25 ℃) using a Land2001A system, and cyclic voltammetry (CV) tests were performed at different scan rates of 0.1 , 0.25, 0.5, and 1 mV s^{-1} in the range of 2.5～3.8 V (potential vs. Na/Na^+). Electrochemical impedance spectroscopy (EIS) measurements were performed in the frequency range of 10^{-1} Hz 10^5 Hz.

3 Results and Discussion

The XRD patterns of NVP/CN-x (x=1, 2, 3, 4) and NVP/C are shown in Figure 1, and they can be indexed to the rhombohedral NASICON structure with space group R3c (PDF standard card #00-62-0345)[32]. It belongs to the hexagonal crystal system, which is consistent with the previous reports, the diffraction peaks of the material are all relatively sharp, and the bottom back of the diffractogram is flat, indicating that good crystallinity of the material, and the XRD pattern shows the absence of heterogeneous peaks, which demonstrates that the purity of the substance is very high. It's worth noting that due to the nitrogen and carbon formation are amorphous, there is no effect on the structure of $Na_3V_2(PO_4)_3$/CN, therefore no diffraction peaks associated with carbon and nitrogen[33]. The peak

intensity of the diffraction peaks while decreasing slightly with the rise in $C_3N_6H_6$ doping is due to the increase in amorphous material and the decrease in crystalline $Na_3V_2(PO_4)_3$ content, which leads to a decrease in crystallinity.

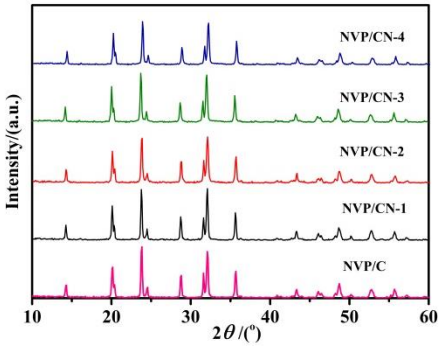

Figure 1 XRD patterns NVP/CN-x (x=1, 2, 3, 4) and NVP/C samples

The morphological features of NVP/CN-x (x=1, 2, 3, 4) composites with varying carbon and nitrogen content are described in Figure 2. From the figure, it can be observed that some fine particles obviously exist on the surface of NVP/CN-x (x=1, 2, 3, 4) particles, and with the increase of carbon and nitrogen content, the particle size of the surface particles of the NVP/CN-x (x=1, 2, 3, 4) composites decreases, and the particle size distribution tends to be more uniform. However, the aggregation of surface particles tends to be more serious with the continuous increase of carbon and nitrogen content, which is the same as that of simple carbon coating, the presence of moderate amount of carbon and nitrogen content can well prevent the growth of particles[34], and the increase of nitrogen content can also make the particle surface too thickly coated, or even bonded, which is unfavorable to the migration of sodium ions. The elemental analysis revealed that the carbon and nitrogen content in the four NVP/CN-x (x=1, 2, 3, 4) composite materials was 6.1wt%, 8.2wt%, 9.9wt%, and 12.0wt%, respectively.

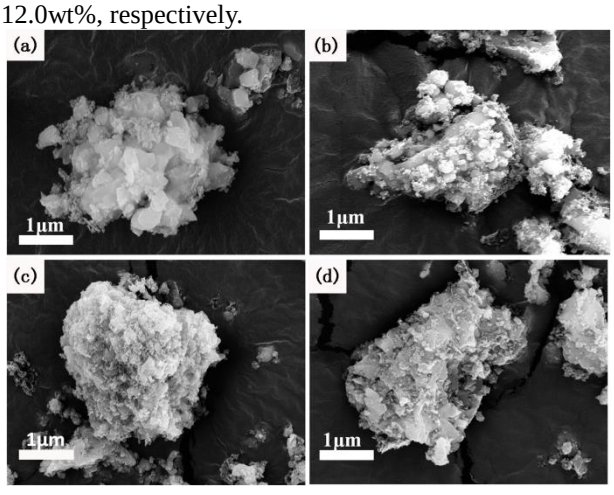

Figure 2 SEM images of NVP-x samples: (a) NVP/CN-1, (b) NVP/CN-2, (c) NVP/CN-3, (d) NVP/CN-4

Figure 3 illustrates the initial charge/discharge curves of NVP/C and NVP/CN-x (x=1, 2, 3, 4) samples obtained at a 0.2 C rate within the voltage range of 2.5～3.8 V (vs. Na^+/Na). As depicted, all samples exhibit prolonged and distinct voltage plateaus. The plateau at 3.4 V (vs. Na^+/Na) corresponds to the reversible phase transition between $Na_3V_2(PO_4)_3$ and $NaV_2(PO_4)_3$. Notably, NVP/CN-2 demonstrates the highest discharge capacity (111.5 mAh/g) and exhibits the narrowest plateau gap between charge and discharge curves, indicative of superior redox kinetics. Due to the different electronegativity between the carbon and nitrogen elements, doping of nitrogen leads to the formation of an n-type matrix. The multi-electron character of nitrogen alters the original electronic balance, generating additional active sites and enhancing electronic conductivity.

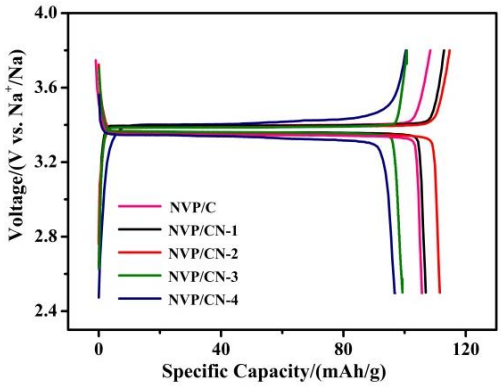

Figure 3 The initial charge-discharge curves of NVP/CN-x (x=1, 2, 3, 4) and NVP/C samples

The rate performance of NVP/C and NVP/CN-x (x=1, 2, 3, 4) composite materials is presented in Figure 4 The electrodes are successively charge and discharge 10 times at each of the 0.2 C～ 20 C rates, and return to the initial rate (0.2 C) after 70 cycles of charge and discharge. Corresponding to the initial charge-discharge cycle, NVP/CN-2 exhibits the better rate performance. It delivers discharge capacities of 111.4, 106.1, 101.4, 97.6, 93.9, 90.5, and 85.0 mAh/g at rates of 0.2 C, 0.5 C, 1 C, 2 C, 5 C, 10 C, and 20 C, respectively. Surprisingly, after undergoing 70 cycles at different rates, the discharge capacity of NVP/CN-2 can recover to 111.2 mAh/g (a retention rate of 99.82%) when the rate is reduced back to 0.2 C. It demonstrates the excellent reversibility of sodium storage. Furthermore, it's observed that NVP/CN-2 exhibits a noticeable enhancement in electrochemical performance compared to NVP/C, particularly at high rates such as 20 C. This enhancement is attributed to the nitrogen doping, which generates more defects in the original carbon layer, facilitating the migration of large sodium ions and aiding in sodium ion diffusion. Conversely, as the carbon and nitrogen content increases further, the rate performance of NVP/CN-x materials deteriorates. It may be due to excessive carbon

and nitrogen content leading to a reduction in the energy density of the cathode material, as well as the encapsulation of the active material, which hinders sodium ion diffusion, collectively resulting in a decline in electrochemical performance[35]. Proper carbon-nitrogen doping contributes to the improvement of the rate performance of material.

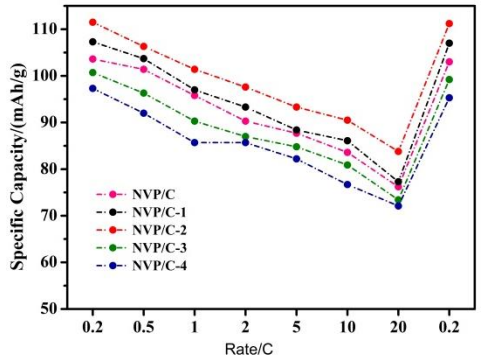

Figure 4 Rate performance of NVP/CN-x (x=1, 2, 3, 4) and NVP/C

Figure 5 illustrates the long-term cycling performance of NVP/CN-x (x=1, 2, 3, 4) and NVP/C samples at a 0.2 C rate. As shown, the retention rates after 1000 cycles for NVP/C and NVP/CN-x are as follows: 80.68%, 97.57%, 96.68%, 90.94%, and 70.45%. Notably, NVP/CN-2 and NVP/CN-3 exhibit the better cycling performance. These experimental findings suggest that defects induced by the nitrogen doping in the carbon layer are advantageous for enhancing electronic conductivity and improving interfacial charge transfer, thereby enhancing cycling stability[36]. However, as the nitrogen content increases, excessive surface defects in the material lead to extensive contact with the electrolyte, resulting in increased side reactions and severe polarization.

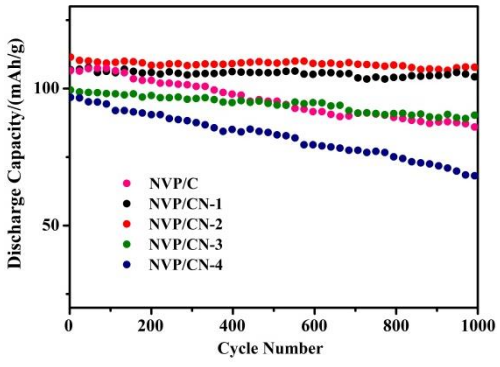

Figure 5 Cycle performance of NVP/CN-x (x=1, 2, 3, 4) and NVP/C

In order to further investigate the electrochemical processes, cyclic voltammetry (CV) tests are performed on NVP/CN-x (x = 1, 2, 3, 4) and NVP/C cathode materials. Cyclic voltammetry tests are performed between 2.5 and 3.8 V at a scan rate of 0.1 - 1 mV/s. All electrodes exhibit a pair of redox peaks at 3.4 V at different scan rates attributed to V^{3+}/V^{4+} redox reactions.[37-38] Figures 6 a and 6 c depict the cyclic voltammetry (CV) curves of NVP/CN-2 and NVP/C samples at scan rates of 0.1, 0.25, 0.5, and 1 mV/s. It is evident that with increasing scan rates, the both samples exhibit higher polarization. In comparison, the oxidation-reduction peaks of NVP/CN-2 are more symmetric and sharp, indicating better reversibility. The Na^+ diffusion coefficients were calculated using the classical Randles-Sevcik equation[39]:

$$I_p = 2.69\times10^5 n^{3/2} S D_{Na}^{1/2} v^{1/2} C_0 \quad (1)$$

Here, I_p represents the peak current (A), n denotes the number of electron transfers, S represents the area of the active material on the electrode, D_{Na} stands for the sodium ion diffusion coefficient, v represents the scan rate, and C_0 represents the concentration of sodium ions in the electrode. Figure 6b displays the linear fit of peak current (I_p) and the square root of the scan rate ($v^{1/2}$). Based on Equation (1), sodium ion diffusion coefficients can be obtained by the slope of the fitted line. The diffusion coefficients for the positive and anode electrodes of NVP/CN-2 are 4.74×10^{-10} and 3.98×10^{-10} $cm^2\ s^{-1}$, respectively, while the corresponding diffusion coefficients of NVP/C are 9.65×10^{-11} and 9.32×10^{-11} $cm^2\ s^{-1}$, demonstrating superior performance compared to previously reported diffusion coefficients[40].

EIS is used to evaluate the kinetic characteristics of NVP/CN-x (x = 1, 2, 3, 4) electrode materials. Measurements are performed in the range of 10^{-1} Hz to 10^5 Hz prior to charging and discharging. The spectra of all samples consist of a semicircle in the high-frequency region and a tilted straight line in the low-frequency region. The semicircle observed in the high-frequency range of the Nyquist plot is attributed to charge transfer resistance (R_{ct}) and the diagonal line in the low frequency region corresponds to the Warburg impedance. The R_{ct} of NVP/C and NVP/CN-x (x = 1, 2, 3, 4) are 380.01, 321.13, 289.16, 534.58, and 626.46 Ω, respectively. Evidently, with the increase of carbon and nitrogen content, the R_{ct} value shows a decreasing and then increasing trend, in which NVP/CN-2 exhibits a lower R_{ct} compared to NVP/C and other coated samples, it is demonstrated that the NVP/CN-2 cathode material possesses a faster charge transfer rate, which is consistent with the previous test results. This is attributable to the fact that the carbon and nitrogen coating enhances the electronic conductivity of the particle surface and increases the electronic contact between the particles, which reduces the charge transfer impedance, but as the carbon and nitrogen content is excessively increased, the platelet adhesion occurs on the surface of the material, which is unfavorable to the charge transfer of the material. It is shown that appropriate nitrogen element doped carbon coatings can promote charge transfer and obtain excellent electrochemical properties.

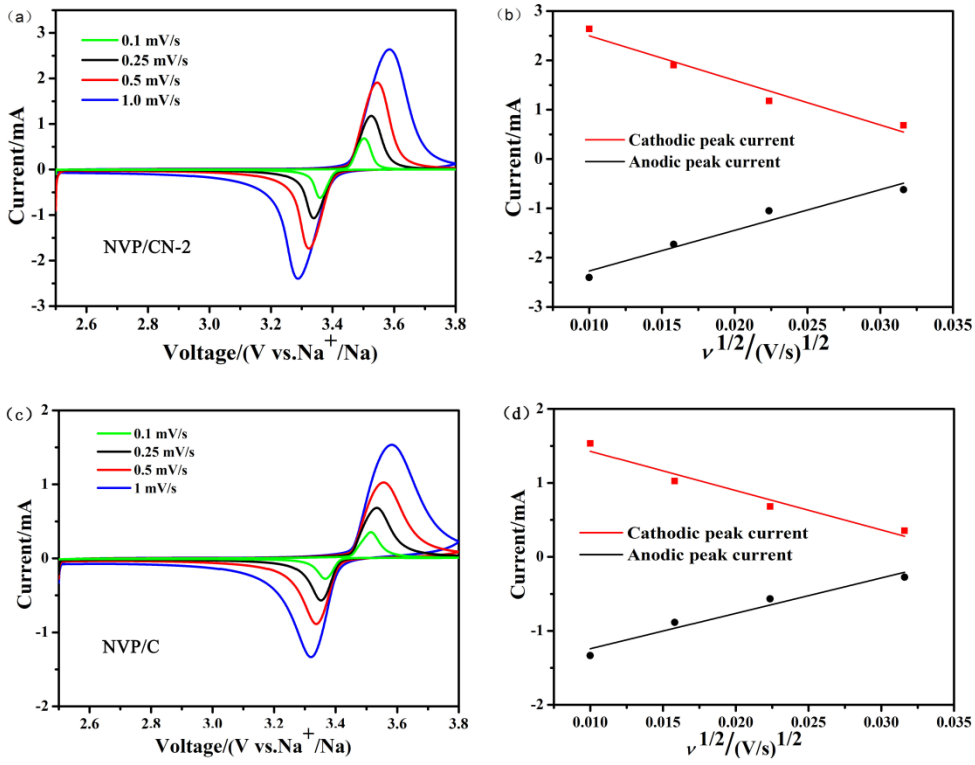

Figure 6 CV curve of NVP/CN-2 and NVP/CN samples in 2.5-3.8 V voltage : (a)(c) At different scanning speeds, (b)(d) The relationship of I_p vs $v^{1/2}$

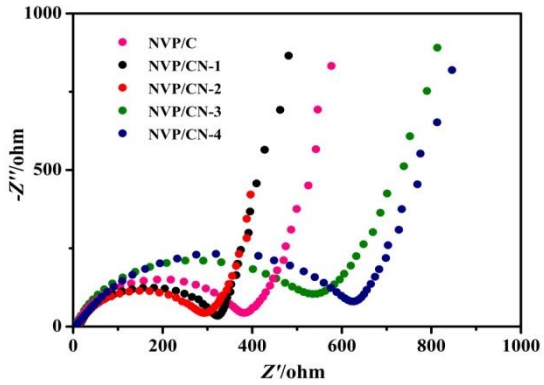

Figure 7 Nyquist plots of NVP/CN-x (x=1, 2, 3, 4) and NVP/C samples

4 Conclusion

This study explored the impact of controlled nitrogen doping in the form of nitrogen -doped carbon layers on $Na_3V_2(PO_4)_3$/C composite materials. The electronic conductivity of the composites is enhanced because the doped nitrogen provides electrons to the carbon matrix. A series of electrochemical tests also demonstrat that an appropriate amount of nitrogen doping plays an important role in the electrochemical performance of the $Na_3V_2(PO_4)_3$/C electrode. When the nitrogen source ($C_3N_6H_6$), is added with an NVP:$C_3N_6H_6$ molar ratio of 2, the discharge capacity reached 111.5 mAh/g. Even after cycling (70 cycle numbers) at various rates (0.2 C to 20 C), the capacity could be restored to 111.2 mAh/g when the rate was reduced back to 0.2 C, with a remarkable retention rate of 99.82%. These results show outstanding cycling performance. The judicious introduction of nitrogen element yields an appropriate number of surface defects, reducing charge transfer resistance, increasing conductivity between particles, and facilitating electron transfer, ultimately resulting in exceptional electrochemical performance.

These authors contributed equally to this work.

References

[1] Wu W W, Sun Z G, He Q, et al. Boosting Lithium-Ion Transport Kinetics by Increasing the Local Lithium-Ion Concentration Gradient in Composite Anodes of Lithium-Ion Batteries [J]. ACS Applied Materials and Interfaces, 2021(13):14752-14758.

[2] Duffner F, Kronemeyer N, Jens T, et al. Post-lithium-ion battery cell production and its compatibility with lithium-ion cell production infrastructure [J]. Nature Energy, 2021(6):123-134.

[3] Pender, J P, Jha G, Youn H, et al. Electrode Degradation in Lithium-Ion Batteries [J]. ACS Nano, 2020(14):1243-1295.

[4] Zhao Y, Kang Y Q, Wozny J, et al. Recycling of sodium-ion batteries [J]. Nature Reviews Materials, 2023(8):623-634.

[5] Yang Z, Li G, Sun J, et al. High performance cathode material based on $Na_3V_2(PO_4)_2F_3$ and $Na_3V_2(PO_4)_3$ for sodium-ion batteries [J]. Energy Storage Materials, 2020(25):724-730.

[6] Klein F, Jache B, Bhide A , et al. Conversion reactions for sodium-ion batteries [J]. Physical Chemistry Chemical Physics, 2023(15):15876-15887.

[7] Philipp A, Pascal H, Bender C L, et al. From lithium to sodium: cell chemistry of room temperature sodium-air and sodium-sulfur batteries [J]. Beilstein J Nanotechnol, 2015(6):1016-1055.

[8] Chen J W, Adi G, Li L, et al. Optimization Strategies Toward Functional Sodium-Ion Batteries [J]. Energy & Environmental Materials, 2023(6):4.

[9] Shi C H, Wang L G, Chen X, et al. Challenges of layer-structured cathodes for sodium-ion batteries [J]. Nanoscale Horizons, 2022(7):338-351.

[10] Xiao J, Li X, Tang K K, et al. Recent progress of emerging cathode materials for sodium ion batteries [J]. Materials Chemistry frontiers, 2021(5):3735-3764.

[11] Li L, Zheng Y, Zhang S L, et al. Recent progress on sodium ion batteries: potential high-performance anodes [J]. Energy & Environmental Science, 2018(11):2310-2340.

[12] Jiang Y, Yang Z, Li W, et al. Nanoconfined Carbon-Coated $Na_3V_2(PO_4)_3$ Particles in Mesoporous Carbon Enabling Ultralong Cycle Life for Sodium-Ion Batteries [J]. Advanced Energy Materials, 2015(5):1402104.

[13] Hwang J Y, Myung S T, Sun Y K. Sodium-ion batteries: present and future [J]. Chemical Society Reviews, 2017(46):3529-3614.

[14] Wu Y C, Meng X H, Yan L J, et al. Vanadium-free NASICON-type electrode materials for sodium-ion batteries [J]. Journal of Materials Chemistry A, 2022(10):21816-21837.

[15] Chen S Q, Wu C, Shen L F, et al. Challenges and Perspectives for NASICON-Type Electrode Materials for Advanced Sodium-Ion Batteries [J]. Advanced Materials, 2017(29):1700431.

[16] Singh K, Chakraborty A, Thirupathi R, et al. Recent advances in NASICON-type oxide electrolytes for solid-state sodium-ion rechargeable batteries [J]. Ionics, 2022(28):5289-5319.

[17] Cheng J, Chen Y, Sun S, et al. $Na_3V_2(PO_4)_3$/C·$Na_3V_2(PO_4)_2F_3$/C@rGO blended cathode material with elevated energy density for sodium ion batteries [J]. Ceramics International, 2021(47):18065-18074.

[18] Salehi A H, Masoudpanah S M, Hasheminiasari M, et al. A solution synthesis of $Na_3V_2(PO_4)_3$ cathode for sodium storage by using CTAB additive [J]. Solid State Ionics, 2020(347):115269.

[19] Jian Z, Zhao L, Pan H, et al. Carbon coated $Na_3V_2(PO_4)_3$, as novel electrode material for sodium ion batteries [J]. Electrochemistry Communications, 2012(14):86-89.

[20] Jiang X M, Liu C C, Tian Z Y, et al. Constructing p-type substitution induced by Ca^{2+} in defective $Na_3V^{2-}xCax(PO_4)_3$/C wrapped with conductive CNTs for high-performance sodium-ion batteries [J]. Dalton Transactions, 2022(51):16145-16157.

[21] Lim S Y, Kim H, Shakoor R A, et al. Electrochemical and Thermal Properties of NASICON Structured $Na_3V_2(PO_4)_3$ as a Sodium Rechargeable Battery Cathode: A Combined Experimental and Theoretical Study [J]. Journal of the Electrochemical Society, 2013(159):A1393-A1397.

[22] Kang J, Baek S, Mathew V, et al. High rate performance of a Na3V2(PO4)3/C cathode prepared by pyro-synthesis for sodium-ion batteries [J]. Journal of Materials Chemistry, 2012(22):20857-20860.

[23] Chen L, Zhao Y, Liu S H, et al. Hard carbon wrapped $Na_3V_2(PO_4)_3$@C porous composite extending cycling lifespan for sodium-ion batteries [J]. ACS Applied Materials and Interfaces, 2017(9):44485-44493.

[24] Chen H, Huang Y, Mao G, et al. Reduced graphene oxide decorated $Na_3V_2(PO_4)_3$ microspheres as cathode material with advanced sodium storage performance [J]. Frontiers in Chemistry, 2018(6):174.

[25] Jiang Y, Zhou X, Li D, et al. Highly Reversible Na Storage in $Na_3V_2(PO_4)_3$ by Optimizing Nanostructure and Rational Surface Engineering [J]. Advanced Energy Materials, 2018(8):1800068.

[26] Wang X X, Wang W W, Zhu B C, et al. Mo-doped $Na_3V_2(PO_4)$3@C composites for high stable sodium ion battery cathode [J]. Frontiers of Materials Science, 2018(12):53-63.

[27] Chen Y J, Xu Y L, Sun X F, et al. Effect of Al substitution on the enhanced electrochemical performance and strong structure stability of $Na_3V_2(PO_4)_3$/C composite cathode for sodium-ion batteries [J]. Journal of Power Sources, 2018(375):82-92.

[28] Ruan Y L, Liu J J, Song S D, et al. Multi-hierarchical nanosheet-assembled chrysanthemum-structured $Na_3V_2(PO_4)_3$/C as electrode materials for high-performance sodium-ion batteries [J]. Ionics, 2018(24):1663-1673.

[29] Zhao Y L, Cao X X, Fang G Z, et al. Hierarchically carbon-coated $Na_3V_2(PO_4)_3$, nanoflakes for high-rate capability and ultralong cycle-life sodium ion batteries [J]. Chemical Engineering Journal, 2018(339):162-169.

[30] Duan W C, Zhu Z Q, Li H, et al. $Na_3V2(PO_4)_3$@C core-shell nanocomposites for rechargeable sodium-ion batteries [J]. Journal Of Materials Chemistry A, 2014(2):8668-8675.

[31] Sun Q, Chen Y J, Tian Z Y, et al. Biomimetic synthesis of craspedia globosa-shaped $Na_3V2(PO_4)_3$ with high performance for sodium ion batteries [J]. Journal of Alloys And Compounds, 2022(909):164719.

[32] Hu F, Jiang X. A stable and superior performance of $Na_3V_2(PO_4)_3$/C nanocomposites as cathode for sodium-ion batteries [J]. Inorganic Chemistry Communications, 2020(115):107860.

[33] Liang X, Ou X, Zheng F, et al. Surface modification of $Na_3V_2(PO_4)_3$ by nitrogen and sulfur dual-doped carbon layer with advanced sodium storage property [J]. ACS Applied Materials & Interfaces, 2017(9):13151-13162.

[34] Zuo P, Cheng G, Wang T, et al. Effects of Carbon on Structure and Electrochemical Performance of Li_2FeSiO_4

Cathode materials for lithium-ion batteries [J]. RSC Advances, 2012(2):6994-6998.

[35] Zhuo H, Wang X, Tang A, et al. The preparation of NaV^{1-} $xCrxPO_4F$ cathode materials for sodium-ion battery [J]. Journal of Power Sources, 2006(160):698-703.

[36] M. Hankel, D. Ye, L. Wang, D.J. Searles, Lithium and sodium storage on graphitic carbon nitride [J], Journal of Physical Chemistry C, 2015(119):21921-21927.

[37] Jiang Y, Zhang H C, Yang H, et al. $Na_3V_2(PO_4)_3$@nitrogen,sulfur-codoped 3D porous carbon enabling ultra-long cycle life sodium-ion batteries [J]. Nanoscale, 2017(9):6048-6055.

[38] Li X M, Wang S J, Tang X, Porous $Na_3V_2(PO_4)_3$ nanoplates for high-performance sodium storage [J]. JournaL of Colloid And Interface Science, 2019(539):168-174.

[39] Du K, Guo H, Hu G, et al. $Na_3V_2(PO_4)_3$ as cathode material for hybrid lithium ion batteries [J]. Journal of Power Sources, 2013(223):284-288.

[40] Luo S H, Li J Y, Bao S, et al. $Na_3V_2(PO_4)_3$/C composite prepared by sol-gel method as cathode for sodium ion batteries [J]. Journal of the Electrochemical Society, 2018(165):A1460-A1465.

Viser Technology Pte. Ltd.
Research and Application of Materials Science
DOI: 10.33142/rams.v7i1.18640

Research Article Open Access

Many-body Interaction Properties and Zero-point Vibration Pressure of Solid Argon Based on Atomic Crystal Configurations

Xingrong ZHENG*, Fengfeng YANG, Haijun CHEN

College of New energy, Longdong University, Qingyang, Gansu, 745000, China

*Corresponding Author: Xingrong ZHENG, E-mail: zhengxingrong2006@163.com

Abstract

Based on atomic crystal configurations, we studied many-body interaction properties of face-centered cubic (fcc) solid argon (Ar) within the atomic distance range of 2.0Å to 3.6Å at T=300 K. The resulting EOS can accurately describe the compression behavior of solid Ar under the experimentally investigated pressure range (0～114GPa). Statistically, 903 $(Ar)_2$ clusters were identified, corresponding to 12 distinct geometric configurations, 861(Ar)3 clusters correspond to 25 distinct geometric configurations, 816 (Ar)4 clusters correspond to 27 distinct geometric configurations, and the calculation results exhibited good convergence. For comparative purposes, the EOS of fcc solid Ar was also calculated using a two-body potential-only approach, which showed excellent agreement with experimental data under relevant pressures. Incorporating three-body terms extended the EOS accuracy to 80 GPa, while the inclusion of four-body terms further improved the precision up to 114 GPa. Higher-order many-body terms are expected to enable accurate interpretation of experimental phenomena in solid Ar above 114 GPa. In addition, when the molar volume is reduced to a fixed value, the zero-point vibration pressure has already reached a certain proportion, then it must be considered and cannot be ignored. This study provides a reliable theoretical model for the study of high-pressure properties and zero-point energy of rare gas solids.

Keywords: *Solid argon; Atomic configuration; Many-body interaction properties*

1 Introduction

Solid argon (*Ar*), as a typical rare gas solid, has attracted extensive theoretical research interest due to its unique electronic and optical properties[1-7]. It also has important application prospects in fields such as cryogenic phonon detectors[5] and dark matter detection, while zero-point vibration energy[6] and other related properties have become key research focuses. Previous studies have explored the EOS of solid *Ar* under different temperature and pressure conditions[2,7], and first-principles calculations have been widely used to analyze its electronic structure and elastic modulus [3,4]. However, the influence of multi-body interactions (especially high-order terms) on the EOS of solid *Ar* under high pressure (exceeding 80 GPa) still needs further refinement[8-15]. Recent scientific research on solid *Ar* has yielded significant advances across extreme condition chemistry, thermophysical property characterization, and applied material sciences[16-22]. A groundbreaking 2025 study by Lawrence Livermore National Laboratory and collaborators revealed that solid argon loses its chemical inertness under conditions mimicking Earth's core-pressures exceeding 1.5 million atmospheres and temperatures above 2,000 Kelvin-reacting with nickel to form a stable ArNi intermetallic compound, which may resolve longstanding geological questions about argon's fate in planetary interiors[21]. In the realm of thermophysical research, a recent study published in the Journal of Molecular Modeling has significantly refined the computational framework for predicting the transport properties of solid Ar (e.g., diffusion coefficient and viscosity). By integrating nuclear spin effects and symmetry constraints into the theoretical model, and leveraging ab initio-derived potential energy curves coupled with the Chapman-Enskog kinetic theory, this work has substantially enhanced the predictive accuracy of transport properties across a broad temperature spectrum[22]. Beyond fundamental research, solid argon-related materials like argyrodite have shown promise in solid-state batteries, with pressure-tolerant anodes reducing dendrite growth and heat generation, and argon's inertness remains critical in advanced manufacturing processes such as bright annealing of

Received on February 3, 2025; Accepted on March 17, 2025

aerospace alloys, where it preserves material integrity and prevents oxidation.

Based on the coupled cluster singles and doubles with perturbative triples (CCSD(T)) method and the aug-cc-pVQZ basis set, we systematically analyzed the geometric structure and potential energy characteristics of $(Ar)_n$ clusters ($(Ar)_2$ to $(Ar)_5$) in the fcc lattice, and quantified the contributions of many-body interactions to the EOS of solid *Ar*, aiming to provide a more accurate theoretical basis for interpreting high-pressure experimental phenomena. The coupled cluster singles and doubles with perturbative triples (CCSD(T)) method has already been applied in previous studies[3,6,23], and it has been proven to be the most accurate and practical method for studying the properties of dense inert elements.

2 Computational Methods

The total energy of solid *Ar* under different molar volumes was expressed as the sum of many-body interaction energies, and the specific form is shown in the following formula[18]:

$$\begin{aligned} E(V) &= E_2(V) + E_3(V) + \cdots \\ &= \frac{1}{2}U_2(o) + \frac{1}{3}U_3(o) + \cdots \\ &= \frac{1}{2}\sum_{i=1}^{n-1} u_2(o,i) + \frac{1}{3}\sum_{i<j=1}^{n-1} u_3(o,i,j) + \cdots \end{aligned} \quad (1)$$

Where $E_n(V)$ represents the *n*-body interaction energy component related to molar volume *V*, $U_n(o)$ denotes the total *n*-body potential energy centered on atom *o*, and $u_n(o, i, j, \ldots)$ is the *n*-body potential energy function between the central atom *o* and surrounding atoms[18].

The pressure is expressed by:

$$P(V,T) = \sum_{n=2}^{+\infty} P_n(V) + P_{zp}(V) + P_{th}(V,T) \quad (2)$$

The pressure corresponding to many-body term is derived from the partial derivative of the energy with respect to volume:

$$P_n(V) = -\frac{\partial E_n(V)}{\partial V}, (n=2,3,4,\ldots) \quad (3)$$

The thermal pressure of solid *Ar* at finite temperature was calculated using the following formula:

$$P_{th}(V,T) = \frac{\gamma 9 k_B T}{V}\left(\frac{\Theta}{T}\right)^{-3}\int_0^{\Theta/T}\frac{x^3}{e^x - 1}dx, \quad (4)$$

where γ is the *Grüneisen* coefficient, k_B is the Boltzmann constant, Θ is the Debye temperature, and *T* is the absolute temperature.

The zero-point vibrational pressure P_{zp} is given by:

$$P_{zp}(V) = \frac{\gamma}{V}E_{zp}, \quad (5)$$

and the zero-point vibrational energy E_{zp} is:

$$E_{zp} = \frac{9}{8}k_B\Theta \quad (6)$$

3 Calculation Results and Discussion

3.1 Geometric configurations of Ar clusters

Based on the established fcc lattice structure of solid *Ar*[19], it analyzed the properties of Ar_2 to Ar_5 clusters, including geometrical configuration, geometrical parameters. Figure 1 showed some geometric configurations of Ar_5 clusters in fcc lattice. The results showed that, all 12 geometric configurations of $(Ar)_2$ clusters are linear, so their structural diagrams are not separately presented. For $(Ar)_3$ clusters, it have 861 (C^2_{42}) atoms and belong to 25 different geometric configurations, $(Ar)_4$ clusters have 816 (C^3_{18}) atoms and belong to 27 different geometric configurations. For $(Ar)_5$ multiple typical configurations were observed. Detailed structural parameters (such as bond lengths and bond angles) of these clusters were recorded to provide a basis for subsequent potential energy calculations.

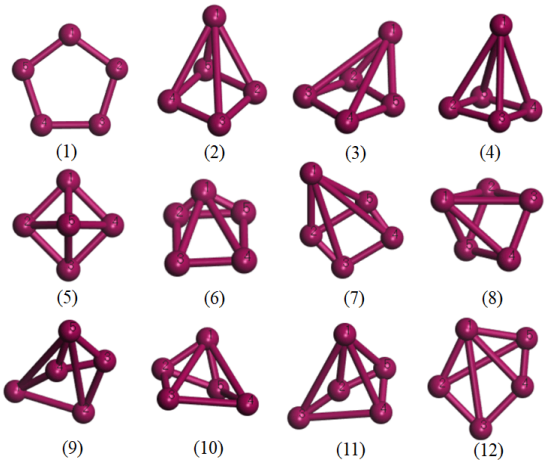

Figure 1 Part of geometric configurations for $(Ar)_5$ clusters in fcc lattice

3.2 Truncation and convergence of many-body potentials

The convergence speed of the many-body expansion series directly affects the computational efficiency of potential energy. For the truncation radius of atomic potentials, the potential energy values tend to stabilize with the increase of the number of neighboring atoms. We analyzed the variation of two-body potential energy $U_2(o)$ and three-body potential energy $U_3(o)$ with the truncation radius at atomic distances of 2.0Å, 2.4Å, 2.7Å, and 3.2Å in the fcc phase, as shown in Figure 2. The results show that when the truncation radius reaches 4.0Å, the two-body and three-body potential energies basically reach saturation, and the number of neighboring atoms corresponding to this radius is 42. Considering the balance between computational accuracy and efficiency, a truncation radius of 4.0Å was selected for subsequent calculations, which can achieve a good approximation effect while avoiding excessive

computational costs. For the atomic distance of 2.0Å, the number of sampling points was set to 200,000 to ensure the reliability of the calculation results.

3.3 Equation of state

In the equation of state calculation, the total pressure $P(V)$ are composed of static pressure P_n, zero-point vibration pressure P_{zp} and thermal pressure P_{th}, which are functions of molar volume V. It was found that the zero-point vibration pressure P_{zp} and thermal pressure P_{th} of solid *Ar* account for less than 5% of the total pressure $P(V)$, but their contributions cannot be ignored in high-precision calculations. This study compared the EOS results of different combinations: the two-, three-, four-body potential pressure, zero-point vibration pressure, thermal pressure ($P_2+P_3+P_4+P_{zp}+P_{th}$), as shown in Figure 3. The results show that, only considering two-body potential, our calculation results are in good agreement with the experimental data[8,20] within a pressure of 15GP. Within the pressure range of 0～80 GPa, the calculation results which considering the two- and three-body potential pressure are in good agreement with the experimental data[8,20]. When the pressure exceeds 80 GPa, the EOS accuracy of the two-, three-body-based combination decreases significantly, while the combination including four-body terms can maintain high precision up to 114 GPa, while the consistency between the calculation results of density functional theory based on the generalized gradient approximation (GGA) and the local-density approximation (LDA) and the experimental data[8,20] in the high-pressure area. Above 114 GPa, the influence of higher-order many-body terms (five-body and above) becomes prominent, and their inclusion is required to accurately interpret the experimental phenomena under ultra-high pressure. In addition, it can be seen from the top right image in Figure 3 that the zero-point vibration pressure and thermal pressure are relatively small, but not negligible within the entire experimental range of pressure.

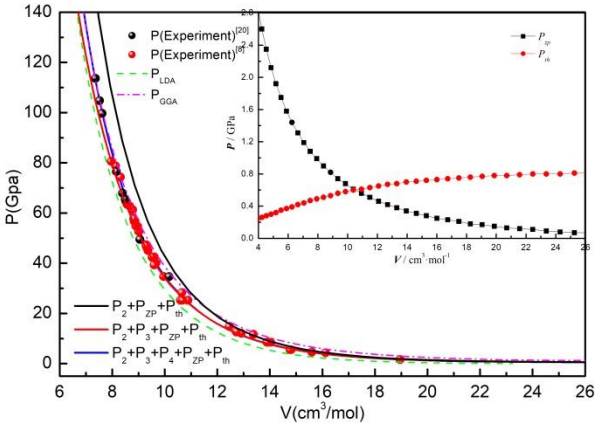

Figure 3 Equation of state for solid *Ar*

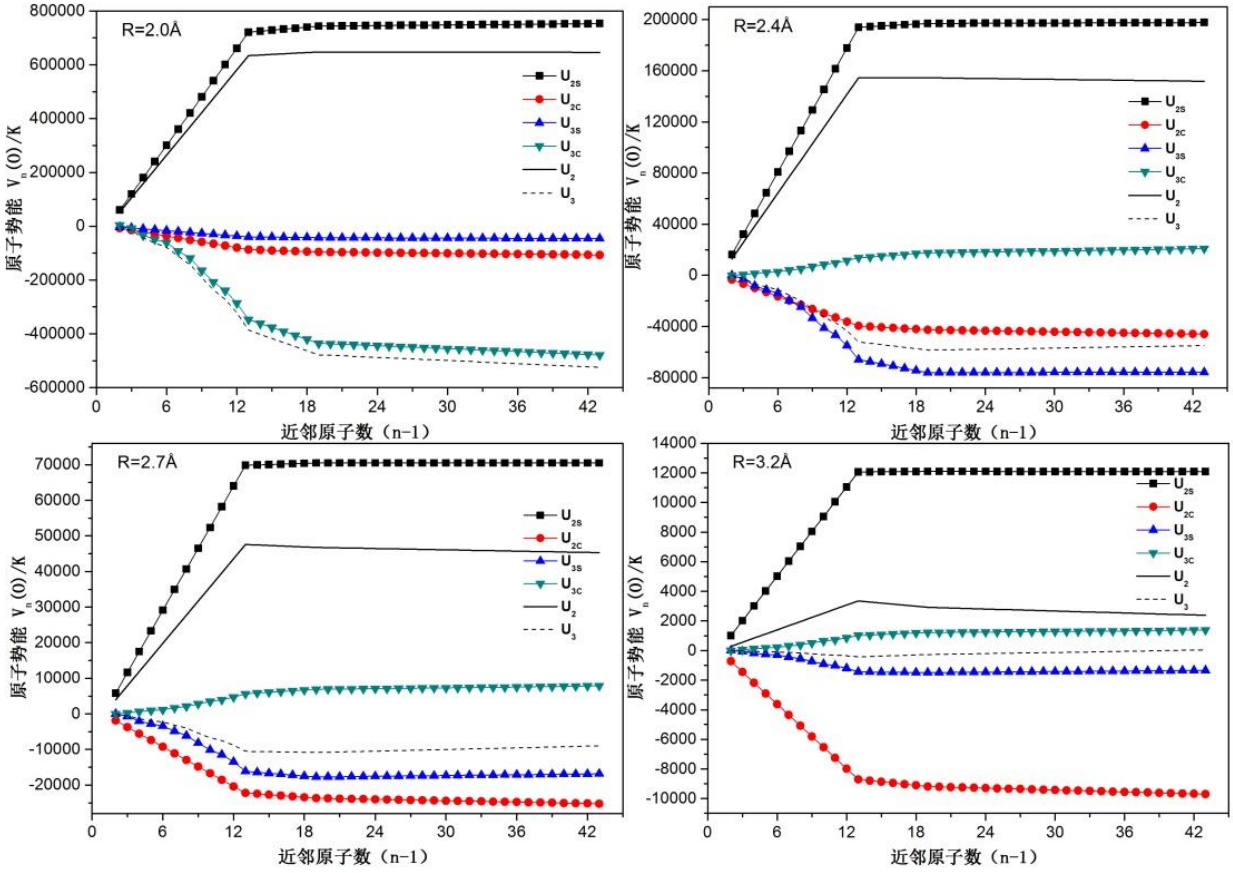

Figure 2 Atomic potential and its many-body components variations with the number of neighbours at R=2.0, 2.4,2.7, 3.2Å in fcc phase

4 Conclusions

Based on the CCSD(T) method and aug-cc-pVQZ basis set, we accurately calculated the two-, three-body and four-body contributions to the cohesive energy and EOS of fcc solid *Ar* within the atomic distance range of 2.0Å to 3.6Å at room temperature (T=300 K). The geometric structures of $(Ar)_2$, $(Ar)_3$, $(Ar)_4$, and $(Ar)_5$ clusters in the fcc lattice were clarified, and their symmetry characteristics and structural parameters were analyzed. The truncation radius of 4.0Å was determined through convergence tests, which balances computational efficiency and accuracy. EOS comparison results show that the model including two-body and three-body terms can accurately describe the compression behavior of solid *Ar* within 80 GPa, and the addition of four-body terms extends the applicable pressure range to 114 GPa. To further improve the EOS accuracy above 114 GPa, it is necessary to consider the contribution of higher-order multi-body interactions. Although the zero-point vibration pressure and thermal pressure are relatively small, but not negligible within the entire experimental range of pressure. Especially, when the molar volume is reduced to a fixed value, the zero-point vibration pressure has already reached a certain proportion, then it must be considered. This study provides a reliable theoretical model for the study of high-pressure properties and zero-point energy of rare gas solids.

Acknowledgement: The research are sponsored by the Youth Talent (team) project of Gansu Province (Grant No. 2025QNTD12), the Natural Science Foundation of Gansu Province (Grant No. 25JRRM001, 23JRRM0755).

References

[1] T. W. Maltby, M. Hammer. Equation of State for Solid Argon Valid for Temperatures up to 300 K and Pressures up to 16 GPa [J]. Journal of Physical and Chemical Reference Data, 2024, 53(4):043102.

[2] X. Xiao, S. Sriskandaruban. Equation of State for Solid Argon Valid for Temperatures up to 760 K and Pressures up to 6300 MPa [J]. International Journal of Thermophysics, 2025, 46(1):1-47.

[3] N. Boucerredj, K. Beggas. First Principle Calculation of Electronic and Optical Properties of Rare Gas Solids Kr and Ar [J]. Acta Physica Polonica A, 2020, 138(3):428-433.

[4] T. T. Ha, D. D. Phuong. Investigation of mean-square displacement and elastic moduli of solid argon up to 85 GPa [J]. Chemical Physics, 2020(539):110928.

[5] Y. Liu, L. Zhang. Cryogenic phonon-detector model with solid argon for detecting dark matter [J]. Chinese Physics C, 2023,47(12):5-13.

[6] X. R. Zheng, H. J. Chen. The zero-point vibration contributions to energy and compressibility of light rare-gas solids [J]. Physica B, 2023(669):415268.

[7] V. N. Nguyen, H. H. Khac. Equation-of-state and melting curve of solid neon and argon up to 100 GPa [J]. Vacuum, 2022(196):110725.

[8] D. Errandonea, R. Boehler, S. Japel, M. Mezouar, and L. R. Benedetti. Structural transformation of compressed solid Ar: An x-ray diffraction study to 114 GPa [J]. Phys. Rev. B., 2006,73(9):092106.

[9] Li J H, Zheng X R, Peng C N. Effect of many-body interactions on the equation of state for solid argon [J]. Journal of Sichuan University. 2016,53(1):131-136.

[10] Freiman Y A, Tretyak S M. Many-body interactions and high-pressure equations of state in rare-gas solids [J]. low temperature physics, 2007,33(6-7):545-552.

[11] I. V. Shchus, D. A. Tyurin, V. I. Feldman. Radiation-induced transformations of isolated dimethyl disulphide molecules in solid argon [J]. Radiation Physics and Chemistry, 2024(11):215.

[12] S. G. Boussahoul, M. Benguerba. Modeling of sputtering from solid surfaces under argon cluster bombardments: comparison with experimental and simulated data [J]. Applied Surface Science, 2025(703):163428.

[13] I. S. Sosulin,V. I. Feldman. Infrared spectrum of CF^{2+} cation in a solid argon matrix [J]. Chemical Physics Letters, 2022(807):140108.

[14] E. I. German, S. B. Tsydypov. Structure of Argon Solid Phases Formed from the Liquid State at Different Isobaric Cooling Rates [J]. Applied sciences-basel, 2024,14(3):1295.

[15] S. L. Chou, S. Y. Lin. Infrared absorption spectra of phenoxide anions isolated in solid argon [J]. Journal of the Chinese Chemical Society, 2022,69(1):133-139.

[16] X. R. Zheng, L. Su. The fitting of three-body potential energy of solid argon [J]. Journal of Physics: Conference Series, 2021,1906(1):012011.

[17] M. Miyaji, B. Radola. Extension of Kirkwood-Buff theory to solids and its application to the compressibility of fcc argon [J]. The Journal of chemical physics, 2021,154(16):164506.

[18] A. N. Singh, J. C. Dyre, U. R. Pedersen. Solid-liquid coexistence of neon, argon, krypton, and xenon studied by simulations [J]. The Journal of chemical physics, 2021,154(13):134501.

[19] X. R. Zheng, G. Q. Li. Investigations of crystal configuration and material properties of high-compressed solid argon [J]. Journal of Qinghai University, 2019,37(6):71-79.

[20] A. P. Jephcoat. Rare-gas solids in the Earth's deep interior [J]. Nature, 1998(393):355.

[21] A. A. Adeleke, M. Kunz. A High-Pressure Compound of Argon and Nickel: Noble Gas in the Earth's Core [J]. ACS Earth and Space Chemistry, 2019,3(11):2517-2524.

[22] F. Bouchelaghem, H. Boutarfa. New determination of the thermophysical properties of argon gas considering nuclear spin and symmetry effects [J]. Journal of molecular modeling, 2025,31(8):215.

[23] X. R. Zheng. Higher-term contributions in the many-body calculation of the compressibility and thermodynamic properties of solid neon [J]. Indian Journal of Physics, 2019,93(12):1579-1589.

Viser Technology Pte. Ltd.
Research and Application of Materials Science
DOI: 10.33142/rams.v7i1.18641

Research Article Open Access

Boron Carbide and Composites in Advanced Energy Storage: Research Progress and Prospects

Zhigang YU[1], Shaoyi SHEN[1], Jifeng WANG[2], Song WU[1], Aoyi DONG[1], Xinhua ZHENG[1], Shikai LIU[1*]

1. School of Materials Science and Engineering, Henan University of Technology, Zhengzhou, Henan, 450001,China
2. Zhengzhou Songshan Boron Industry Technology Co., Ltd., Zhengzhou, He'nan, 452470, China

[*]***Corresponding Author:*** *Shikai LIU, E-mail: shikai_liu@haut.edu.cn*

Abstract

Boron carbide (B4C) and its composite materials demonstrate versatile applicability in energy storage technologies, particularly within new energy battery systems. This review systematically examines recent advances in their battery applications. Commencing with an analysis of B4C's distinctive physicochemical properties, crystal structure, and synthesis methodologies, we critically evaluate its implementation in lithium-ion batteries (LIBs), sodium-ion batteries (SIBs), lithium-sulfur (Li-S) batteries, and fuel cells. The discussion substantiates how B4C-based materials augment critical battery performance metrics. Finally, development challenges and future research trajectories are outlined. We anticipate that through targeted performance optimization, innovative processing techniques, advanced interface engineering, and cross-disciplinary integration, B4C composites will unlock broader applications in next-generation energy storage systems.

Keywords: *Boron carbide(B4C); Composite materials; Advanced energy storage; New energy batteries; Application advances*

1 Introduction

The urgent global demand for sustainable energy solutions has propelled technological innovation in advanced energy storage systems to critical significance. Among emerging materials, boron carbide (B4C) and its composites have garnered substantial research interest owing to their exceptional properties, including ultra-high hardness (≈30 GPa), elevated melting point (> 2400 ℃), low density (2.52 g/cm^3), superior chemical inertness, and notable neutron absorption capacity[1-3]. As a semiconductor with demonstrated thermoelectric potential [4], B4C is now transitioning from traditional applications toward advanced electrochemical energy storage, revealing compelling capabilities[5].

Although research on B4C in battery technologies remains developmental, its foundational merits—exceptional chemical resistance, structural stability, tunable electrical conductivity, catalytic activity, and favorable mass density[6]—have been preliminarily validated in lithium-ion batteries (LIBs)[7] and fuel cells[8]. These attributes position B4C as a promising candidate to address core challenges in contemporary energy storage, such as limited cycle stability, constrained energy density, safety concerns, and cost inefficiencies[9,10].

Despite notable progress, critical scientific questions and technical barriers persist in the application of B4C composites. Deeper exploration of their electrochemical roles promises not only to extend functional boundaries but also to overcome existing bottlenecks in energy storage technology, thereby accelerating the development of efficient, stable, and sustainable systems. Consequently, a systematic review of B4C-based materials in new energy batteries, coupled with critical assessment of their capabilities and limitations, carries significant implications for next-generation battery innovation.

2 Overview of Boron Carbide and Its Composite Materials

2.1 Structure and properties of boron carbide

Boron carbide (B4C), with the chemical formula B4C, exhibits a broad homogeneity range (B4C-B5-10C). Its crystal structure belongs to the rhombohedral system (space group D3d5-R$\bar{3}$m), with lattice parameters *a* = 0.519 nm, *c* = 1.212 nm, and α = 66.3° [11] (Figure 1). At the atomic level, it consists of B_{12} icosahedra interconnected by linear C-B-C chains[12-14]. This unique

Received on April 11, 2025; Accepted on May 29, 2025

configuration confers exceptional properties including high hardness and high melting point.

The chemical bonds exhibit strong covalent character, with high B-C bond energy, rendering the structure stable under high temperatures, high pressures, and chemical corrosion. Furthermore, boron carbide demonstrates semiconducting behavior (electrical conductivity σ ≈ 100 S/cm), good electrical conductivity, and catalytic activity[6]. Collectively, these properties underpin its diverse applications across multiple fields.

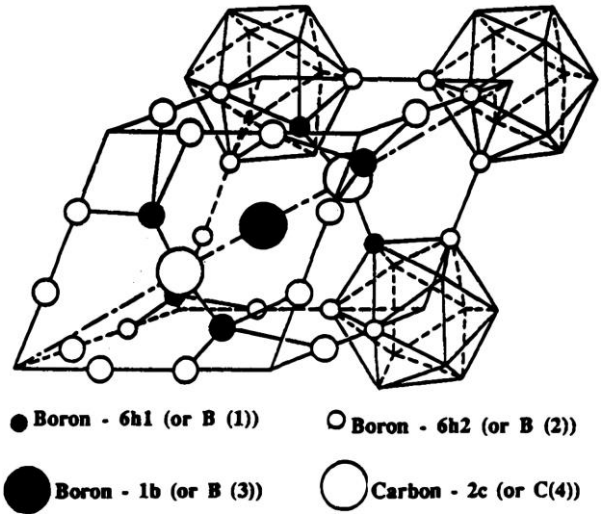

Figure 1 Rhombohedral crystalline structure of boron carbide[11]

2.2 Overview of boron carbide preparation methods

Boron carbide (B4C) is synthesized through diverse methods, with carbothermal reduction being the most prevalent industrial process. This technique involves reacting stoichiometric mixtures of boric oxide (B2O3) and carbon sources (e.g., coke, graphite) in electric furnaces at 2000～2500 ℃, following the reaction: 2B2O3+7C→B4C+6CO↑. Valued for its mature technology and cost-effectiveness, it remains the preferred method for large-scale production[15]. Self-propagating high-temperature synthesis (SHS) utilizes exothermic reactions between boron and carbon powders, where compacted powder mixtures are ignited locally to propagate rapid combustion waves that yield B4C. While SHS offers advantages of rapid kinetics and low energy consumption, it faces challenges in controlling product purity and particle size[16]. Emerging techniques include mechanochemical synthesis, which employs mechanical forces to induce chemical reactions[17], and sol-gel processing that achieves atomic-level mixing through colloidal precursors to produce high-purity nanoscale B4C powders[18,19]. However, these advanced methods are currently confined to laboratory-scale optimization due to cost constraints limiting industrial adoption. Comparative characteristics of common B4C synthesis methods—including principles, process parameters, and key features—are systematically summarized in Table 1.

Table 1 Common Synthesis Methods and Characteristics of Boron Carbide

Synthesis Method	Principle	Process Parameters	Key Features	Development Stage
CarbonThermal Reduction	B_2O_3 reacts with carbon sources (coke, graphite, etc.) to produce B_4C and carbon monoxide.	In an electric furnace at high temperatures (2000 ℃ to 2500 ℃), the reaction is: $2B_2O_3+7C→B_4C+6CO↑$	Mature technology and relatively low cost	The preferred choice for large-scale industrial production
Self-propagating High-temperature Synthesis (SHS)	Maintain the reaction using the exothermic chemical reaction of the reactants themselves. Mix boron powder and carbon powder, press into a block, and ignite one end. Once ignited, the reaction will spread on its own.	Self-sustaining propagation upon ignition	he reaction is fast, energy consumption is low, but it is difficult to control the purity and particle size of the product.	Control difficulties exist in practical applications.
Mechanochemical	Chemical reactions are induced via mechanical force.		Currently in the laboratory research optimization phase, with relatively high costs.	Laboratory stage, not yet widely used
Sol-gel	Atomic-level mixing is achieved via the sol-gel process		High-purity, nanoscale boron carbide powder can be prepared, but it is currently in the laboratory research and optimization stage and is relatively expensive.	Laboratory stage, not yet widely used

2.2 Overview of boron carbide preparation methods

Boron carbide (B4C) is synthesized through diverse methods, with carbothermal reduction being the most prevalent industrial process. This technique involves reacting stoichiometric mixtures of boric oxide (B2O3) and carbon sources (e.g., coke, graphite) in electric furnaces at 2000 ～ 2500 ℃, following the reaction: $2B_2O_3+7C \rightarrow B_4C+6CO\uparrow$. Valued for its mature technology and cost-effectiveness, it remains the preferred method for large-scale production[15]. Self-propagating high-temperature synthesis (SHS) utilizes exothermic reactions between boron and carbon powders, where compacted powder mixtures are ignited locally to propagate rapid combustion waves that yield B4C. While SHS offers advantages of rapid kinetics and low energy consumption, it faces challenges in controlling product purity and particle size[16]. Emerging techniques include mechanochemical synthesis, which employs mechanical forces to induce chemical reactions[17], and sol-gel processing that achieves atomic-level mixing through colloidal precursors to produce high-purity nanoscale B4C powders[18,19]. However, these advanced methods are currently confined to laboratory-scale optimization due to cost constraints limiting industrial adoption. Comparative characteristics of common B4C synthesis methods—including principles, process parameters, and key features—are systematically summarized in Table 1.

2.3 Analysis of application potential for boron carbide and its composites

The distinctive properties of boron carbide (B4C) and its composites have demonstrated significant value in traditional applications. Notable examples include B4C /Al composites utilized in aerospace thermal management components and electronic packaging[20], as well as ceramic-matrix composites (e.g., B4C /SiC). Silicon carbide (SiC) ceramics inherently exhibit exceptional high-temperature resistance and oxidation stability[21], when composited with B4C, these materials achieve further enhanced thermal capabilities, maintaining high strength and hardness above 1500 ℃—critical for ultra-high-temperature thermal protection systems and extreme-environment components in nuclear reactors. Advancing research into material characteristics has progressively revealed their burgeoning potential in emerging fields, with particular emphasis on applications within new energy batteries.

The development of new energy batteries faces critical challenges including limited cycle life, constrained energy density, and safety concerns. Boron carbide addresses these issues through its high chemical stability, favorable electrical conductivity, exceptional catalytic activity, and robust structural stability—offering novel material-based solutions. These properties demonstrate significant compatibility across lithium-ion batteries (LIBs), sodium-ion batteries (SIBs), lithium-sulfur (Li-S) batteries, and fuel cells, positioning B4C-based materials as a prominent research focus in electrochemical energy storage.

3 Research on Applications of Boron Carbide and Its Composites in New Energy Batteries

3.1 Lithium-ion batteries

In lithium-ion batteries (LIBs), boron carbide (B4C) and its composites demonstrate distinctive advantages. Pure B4C exhibits lithium-ion storage potential owing to its unique crystal structure and electronic properties[22]. Research confirms that in lithiated boron carbide crystals, Li ions occupy interstitial sites above or below linear C-B-C chains, forming reversible ionic bonding interactions with boron and carbon atoms[23].

Chen et al.[24] proposed an innovative composite structure featuring boron carbide (B4C) as a conductive rigid skeleton supporting silicon. Micron-sized Si (1～5 μm) and B4C (1～7 μm) powders were initially blended in controlled ratios (Figure 2-a), followed by high-energy ball milling (HEBM). During this process, the high-Mohs-hardness B4C particles functioned as nano/micro-milling media, effectively fragmenting Si into sub-10 nm particles while simultaneously reducing their own size to 100～300 nm. These in-situ generated nano-Si particles became intimately anchored onto B4C surfaces, forming Si-coated B4C core-shell structures (Si/ B4C) (Figure 2-b). Subsequent planetary ball milling (PBM) of Si/ B4C with graphite induced mechanical exfoliation and uniform encapsulation of the composites by graphite layers, yielding a final triple-layered core-shell-shell architecture (Si/ B4C /graphite, SBG) (Figure 2-c). The outer few-layer graphene coating substantially enhanced electrical conductivity and structural stability while facilitating stable solid electrolyte interphase (SEI) formation. The optimized SBG433 anode (Si: B4C:graphite= 4:3:3) delivered exceptional performance: 94% capacity retention after 100 cycles at 0.3 C and a specific capacity of ≈822 mAh/g based on total electrode mass (including binder and conductive additives), underscoring the critical role of synergistic material-structure co-design strategies in developing high-performance lithium-ion batteries.

Boron carbide (B4C) plays a pivotal role in designing high-capacity anodes for lithium-ion batteries (LIBs) due to its unique mechanical and electrochemical properties. Su et al.[25] innovatively engineered a hierarchical SnS_2/ B4C @OUCNTs composite anode, demonstrating a tripartite synergistic mechanism of B4C involving mechanical buffering, electrical enhancement, and interfacial stabilization. This composite—synthesized via chemical vapor deposition and solvothermal methods—features open-ended carbon nanotubes (OUCNTs) as a conductive skeleton with B4C

nanoparticles as an interfacial buffer. Experiments revealed that B4C's ultrahigh hardness (Mohs 9.3～9.5) and elastic modulus (～450 GPa) effectively dissipate lithiation-induced stress in SnS_2, reducing electrode volume expansion by 55%. Its semiconducting behavior ($\sigma \approx 100$ S/cm) synergizes with OUCNTs to construct a 3D conductive network, decreasing interfacial charge-transfer resistance by 67% and enabling a reversible capacity of 620 mAh/g at 5 A/g. Theoretical calculations further revealed charge redistribution (adsorption energy $\Delta E_{ads} \approx$ -2.1 eV) at B4C - SnS_2 heterointerfaces,optimizing Li ion adsorption sites and reducing diffusion barriers by 46% (0.28 eV → 0.15 eV). Additionally, B4C 's chemical inertness inhibits direct SnS_2-electrolyte contact, suppressing polysulfide dissolution and uncontrolled SEI growth, thereby elevating coulombic efficiency to 99.3% with ＞85% capacity retention after 200 cycles. This work validates B4C 's multifunctional coupling effects and establishes a "rigidity-flexibility integration" strategy for developing high-energy-density (＞500 Wh/kg) LIBs with extended cycling (＞ 500 cycles), extendable to other volume-sensitive anodes (e.g., metal oxides/alloys) through heterointerface engineering for substantial practical implementation.

However, pure boron carbide (B4C) faces limitations as an electrode material, including suboptimal electrical conductivity and restricted Li ion diffusion kinetics. To address these constraints, researchers have integrated B4C with diverse materials, yielding significant performance enhancements in LIBs. For instance, B4C -graphene composites leverage graphene's exceptional electrical properties—boosting composite conductivity by several orders of magnitude—while its 2D flexible architecture buffers volume changes during cycling, mitigating electrode pulverization and delamination to enhance structural integrity. Tan et al.[26] systematically investigated B4C ceramics modified with graphene nanoplatelets (GNPs) and Ti_3AlC_2 sintering additives via spark plasma sintering. Using 0～5 vol% GNPs alongside in-situ formed TiB_2 conductive phases (derived from Ti_3AlC_2 decomposition), they fabricated dense B4C composites with superior electrical/thermal conductivity and mechanical properties. The study revealed that GNPs establish long-range conductive pathways via ultrahigh in-plane carrier mobility (～10^5 $cm^2/V \cdot s$), while TiB_2 particles act as localized "conductive nodes" at interfaces-synergistically elevating bulk conductivity by 4 ～ 6 orders of magnitude with a percolation threshold of 1～2 vol%. This breakthrough overcame B4C's intrinsic insulating nature, enabling its first demonstrated electro-discharge machining (EDM) capability. Conductive atomic force microscopy (C-AFM) confirmed continuous conductive networks formed by GNPs/ TiB_2, effectively reducing grain boundary barriers and optimizing charge carrier transport.

Ding et al.[27] systematically elucidated the mechanistic role of boron carbide monolayers (BCx) as lithium-ion battery anodes through integrated first-principles calculations and experimental validation. Their study revealed that interconnected BC5 hexatomic ring networks provide optimal Li ion migration pathways, with unique charge redistribution characteristics reducing the Li ion diffusion barrier to 0.25 eV—significantly lower than graphite's 0.3～0.5 eV—thereby substantially enhancing ionic transport kinetics. Experimentally, BC3/TiN composites demonstrated exceptional rate capability, maintaining a specific capacity of 1,120 mAh/g at 10C with 98.7% Coulombic efficiency. The B-B interatomic distance within BCx monolayers exhibits positive correlation with theoretical capacity; when expanded to 2.8 Å, Li ions engage in multilayer intercalation, enabling a theoretical capacity of 2,600 mAh/g (≈ 7× graphite's capacity). Synthesized BC5 monolayers delivered an initial discharge capacity of 1,850 mAh/g at 0.1C while retaining ＞85% capacity after 500 cycles.

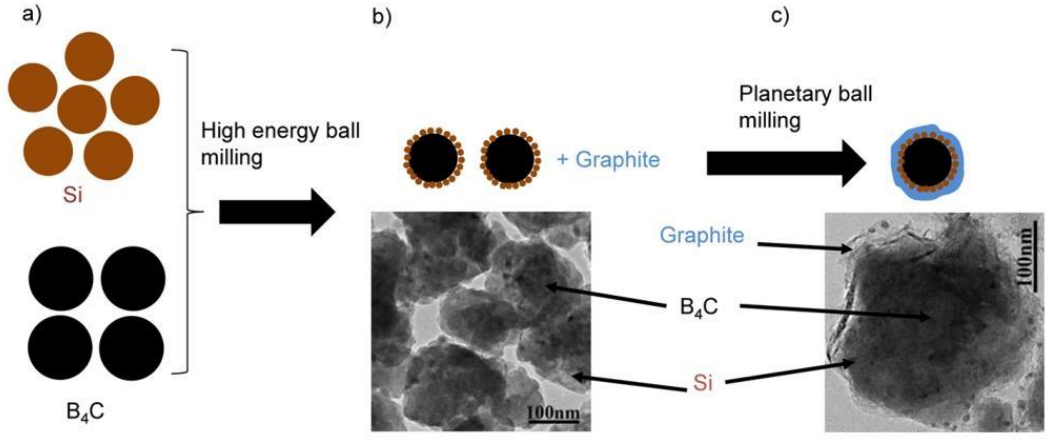

Figure 2 Schematic diagram of the synthesis process of conductive-rigid-skeleton-supported Si with TEM images for the intermediate product of Si/ B4C and the final SBG product. (a) Starting materials of micron-sized B4C and Si. (b) Schematic diagram of the Si/B4C core-shell structure and TEM image. (c) Schematic diagram of the SBG structure and TEM image[24]

3.2 Sodium-ion batteries

In sodium-ion battery (SIB) systems, boron carbide (B4C) and its composites demonstrate significant compatibility. SIBs, leveraging abundant sodium resources and low cost, represent promising contenders for large-scale energy storage. Compared to Li ion (radius ≈0.076 nm), Na ion exhibits a larger ionic radius (≈0.102 nm), necessitating electrode materials with more expansive and stable ion diffusion pathways. B4C's unique crystal structure addresses this requirement through interstitial sites within its 3D framework that facilitate Na ion transport.

Hussain et al. [28] employed density functional theory (DFT) calculations to investigate 3D-B6 C6 porous crystals, revealing metallic behavior with delocalized electrons along B-C-bonded porous channels that confer exceptional electrical conductivity.

Crucially, During the charging and discharging process of sodium-ion batteries, electrode materials also face the problem of volume expansion and contraction. The high structural stability of boron carbide can effectively suppress material pulverization and peeling caused by volume changes, maintain the integrity of the electrode, and ensure the cycle life of the battery. In addition, the good chemical stability of boron carbide allows it to adapt to the electrolyte system of sodium-ion batteries, making it unlikely to undergo side reactions with the electrolyte, reducing internal self-discharge of the battery, and improving the overall performance of the battery.

Zhang et al. [29] synthesized VSe_2/B4C@HCG composites via high-energy ball milling, anchoring VSe_2 and B4C nanoparticles onto highly conductive graphene (HCG). B4C's high hardness suppressed VSe_2 aggregation and volume deformation while synergizing with graphene to enhance charge transfer kinetics (Figure 3). The composite delivered 407.5 mAh/g after 450 cycles (98.5% Coulombic efficiency) and maintained 251.6 mAh/g after 1000 cycles, with significantly superior rate capability versus controls. This work demonstrates B4C's dual role in physical confinement and structural scaffolding to alleviate volume changes, providing new design principles for high-performance SIB anodes.

Sun et al. [30] fabricated a flexible binder-free anode for sodium-ion batteries (SIBs) through high-energy ball milling and free-standing processing, producing B4C /Sn/acetylene black@reduced graphene oxide (B4C /Sn/AB@rGO) films. Their study revealed B4C's multifunctional roles: as a high-hardness conductor, it structurally supports Sn particles while refining micron-sized Sn into nanoscale domains during milling, shortening electron pathways and enhancing overall conductivity. Synergistically with rGO, B4C forms a robust framework buffering Sn's extreme volume changes (～520%) during cycling, suppressing particle aggregation and electrode pulverization to extend cycle life. AB encapsulates B4C /Sn, accelerating electrolyte infiltration and stabilizing solid electrolyte interphase (SEI) formation, while rGO interconnects components as an "electrical nexus" to establish efficient electron transport networks and improve reaction kinetics. The composite delivered 393.4 mAh/g at 0.1 A/g, retained 155.5 mAh/g after 500 cycles at 1 A/g, and maintained 201.5 mAh/g over 50 cycles in full cells at 0.1 A/g, validating B4C's efficacy in optimizing electrode architecture and electrochemical performance.

3.3 Lithium-sulfur batteries

Lithium-sulfur batteries (Li-S) have emerged as a promising candidate for next-generation energy storage technology due to their high theoretical energy density (2567 Wh/kg) and low cost [31-33]. However, they face core challenges such as polysulfide shuttling, slow reaction kinetics, and sulfur volume expansion [34-35]. Boron carbide enhances the cycling stability, rate performance, and energy density of lithium-sulfur batteries through chemical adsorption, catalytic activity, and structural synergy.

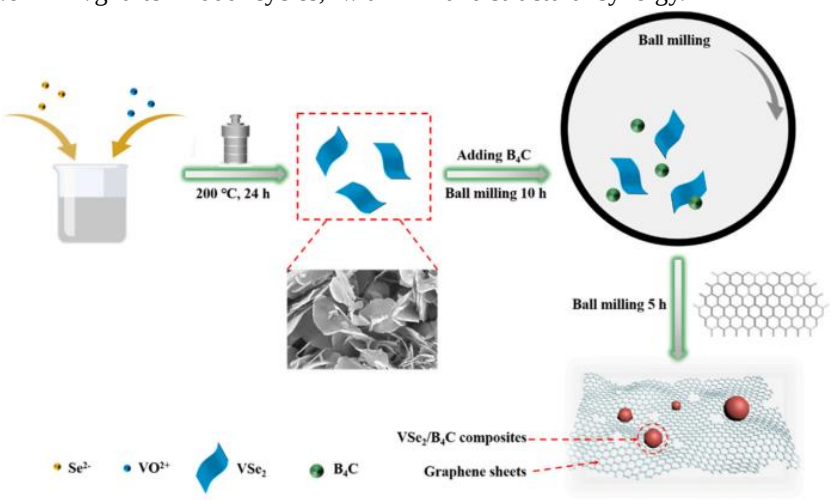

Figure 3 Schematic preparation of the synthesis of $VSe2/B_4C$@HCG[29]

Song et al. [36] designed a flexible self-supporting lithium-sulfur battery cathode BC-NWs@ACT/S/rGO (Figure 4-b), using B4C nanowires as a rigid skeleton combined with porous active cotton textile (ACT) and reduced graphene oxide (rGO), effectively addressing the issues of polysulfide shuttling and volume expansion. B4C nanowires provide mechanical support due to their high hardness and chemical stability, while the porous structure enhances sulfur loading capacity and suppresses volume expansion. Their interaction with polysulfides reduces the diffusion coefficient, and experiments and simulations confirm the suppression of the shuttle effect. B4C and rGO synergistically form a conductive network, with rGO acting as an adaptive protective layer to buffer sulfur volume changes—molecular dynamics simulations (Figure 4-a) illustrate the atomic configuration of the BC-NWs/S/graphene cylindrical structure during charge-discharge cycles. This cathode exhibits outstanding performance: over 1,000 cycles at 1.5 mA/cm², with a capacity decay rate of 0.056% per cycle, an initial discharge capacity of 963 mAh/g, and an increased capacity of 1,395 mAh/g after 50 cycles, demonstrating exceptional rate performance; The assembled flexible battery remains stable under both normal and bent conditions, successfully illuminating an LED, laying the foundation for the development of high-performance flexible energy storage devices.

Luo et al. [37] used a catalyst-assisted process to grow B4C nanowires in situ on the surface of carbon nanofibers (CNF), constructing a self-supporting bifunctional cathode substrate (B4C@CNF), which significantly improved the performance of lithium-sulfur batteries. B4C nanowires form strong chemical adsorption with polysulfides via S-B and S-C bonds, with a binding energy as high as 12.51 eV (Figure 5-b), far exceeding the 1.18 eV of traditional carbon materials, effectively suppressing polysulfide dissolution and shuttling (Figure 5-a). Theoretical calculations show that different B4C crystal faces exhibit distinct adsorption mechanisms (Figure 5-d), and the adsorption process is accompanied by significant electron transfer (Figure 5-e); Bader charge analysis of S atoms further indicates that the charge changes of S atoms after adsorption are correlated with the binding energy (Figure 5-c). Additionally, the catalytic effect of B4C accelerates the redox reaction of polysulfides, increasing the lithium ion diffusion coefficient to 1.3×10^{-7} cm²/s, thereby improving rate performance. B4C@CNF achieves high sulfur loading (10.3 mg/cm²) and content (70 wt%) without requiring additional current collectors or binders. Experimental results show that the battery maintains an 80% capacity retention rate after 500 cycles at 1C and exhibits a reversible capacity of 304 mAh/g at 4C; High-sulfur-load batteries achieve an areal capacity of 9 mAh/cm², with a capacity retention rate of 82%～95% after 100 cycles; soft-pack batteries with a sulfur load of 200 mg exhibit a capacity of 625 mAh/g and an energy efficiency of 90% after 50 cycles. This design offers new insights for the practical application of high-energy-density lithium-sulfur batteries.

Zhang et al. [38] used a catalyst-assisted process to grow B4C nanoparticles in situ on the surface of activated cotton fibers (ACF), constructing a bifunctional cathode substrate (B4C-ACF), and prepared S/B4C-ACF electrodes by loading sulfur via melt diffusion. Combining SEM, TEM, XRD, XPS, and electrochemical testing (CV, rate performance, cycling stability, EIS), they systematically investigated the adsorption capacity of B4C for polysulfides, its catalytic activity, and the synergistic structural effects. The study revealed that B4C nanoparticles strongly chemically adsorb polysulfides via surface B-S and C-S bonds, inhibiting their dissolution and shuttle effects. Experimental and theoretical calculations confirmed that their adsorption capacity significantly outperforms that of pure ACF substrates. Additionally, B4C's high conductivity and active sites accelerate the conversion reaction of polysulfides, reducing overpotential (from 300 mV to 180 mV) and enhancing lithium ion diffusion efficiency, enabling the battery to maintain a reversible capacity of 928 mAh/g even at a 3C rate. The ACF network provides a rapid electronic transport pathway, while B4C nanoparticles enhance mechanical stability and mitigate sulfur volume expansion, collectively achieving high sulfur loading (3.0 mg/cm²) and excellent cycling stability. Electrochemical testing shows that the battery achieves an initial capacity of 1415 mAh/g at 0.1C and a reversible capacity of 928 mAh/g at 3C, with significantly superior rate performance compared to the control group (S/ACF). After 3000 cycles at 1C, the capacity decay rate is only 0.012% per cycle, with a coulombic efficiency as high as 99.24%, demonstrating ultra-long cycle life. XPS and Raman analysis indicate that B4C forms B-S and C-S bonds with polysulfides, suppressing the shuttle effect and promoting reaction kinetics; EIS shows that the charge transfer resistance of the B4C-ACF electrode is significantly reduced, confirming its efficient charge transport capability. This study successfully addresses the polysulfide shuttle and reaction kinetics issues in Li-S batteries through the design of a B4C-ACF dual-functional substrate. The chemical adsorption, catalytic activity, and synergistic interaction of boron carbide with ACF significantly enhance the battery's cycle stability, rate performance, and energy density, providing a new strategy for the development of long-life, high-energy-density Li-S batteries.

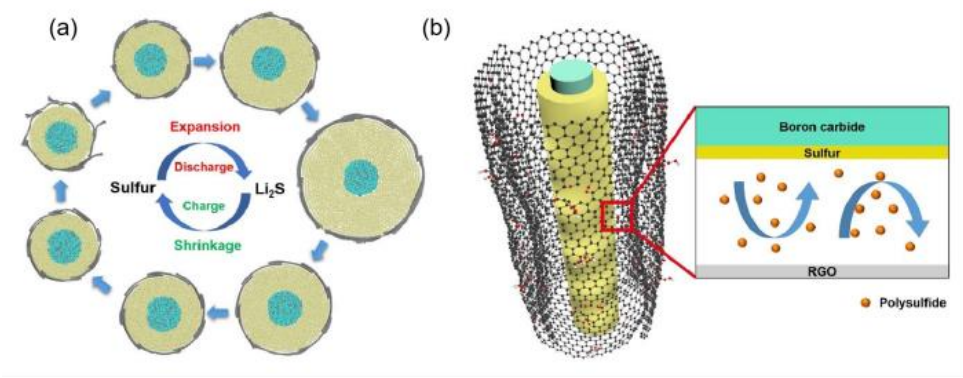

Figure 4 (a)MD snapshots of the atomic configurations representing a cross-section of the BC-NWs/S/graphene cylindrical structure in a cycle of charge/discharge process.(b)Schematic illustration of a representative volume element of BC-NWs@ACT/S/rGO electrode[36]

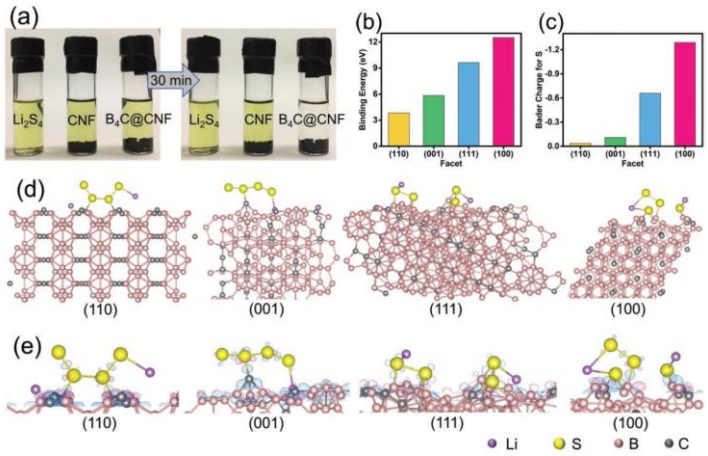

Figure 5 (a) Digital photos of polysulfide adsorption tests.(b) Binding energy and (c) Bader charge for S atoms regarding different B4C@CNF facets.(d) Binding geometry and (e) electron charge transfer when Li2S4 adsorbs on different B4C facets[37]

3.4 Fuel cells

In the research and application of fuel cells, the selection of materials is of critical importance. Boron carbide (B4C) is a highly stable covalent compound. Due to its chemical stability, it is an ideal material for use as a catalyst support, enhancing the catalyst's activity, stability, and resistance to poisoning [39]. Its exceptional high-temperature resistance, high electrical conductivity, excellent chemical stability, high hydrophilicity, and rich surface chemical properties make it a promising candidate material in the field of fuel cells [40]. Zhu et al. [41] conducted a systematic review of the application progress of superhard carbides such as diamond, silicon carbide (SiC), and boron carbide (B4C) in fuel cell catalysis, exploring the advantages of boron carbide as a carrier material and related research findings. Research indicates that boron carbide, with its high chemical stability, conductivity, and surface activity conferred by its strong covalent bond structure, is an ideal alternative to traditional carbon carriers.

Grubb et al. [42] conducted innovative research on fuel cell electrocatalyst supports, using B4C as the platinum-based catalyst support material. They prepared Pt/B4C composite catalysts via chemical adsorption and systematically evaluated their performance in hydrocarbon fuel cells using BET specific surface area testing and in situ electron microscopy analysis. The study demonstrated that the boron-doped carbon carrier significantly enhances platinum's catalytic activity. At 150 ℃ in phosphoric acid electrolyte, the Pt/B4C anode achieved an electro-oxidation current density of 5 mA/mgPt for propane, which is 9 times higher than that of mechanically mixed platinum black catalysts (0.6 mA/mgPt). Additionally, under the same surface coverage, the Pt/B4C composite catalyst demonstrated superior sintering resistance compared to graphite carriers. Experimental data show that the boron-doped carbon carrier optimizes metal-carrier interactions, increasing the actual active area utilization of platinum by 2.7 times (9.3 vs. 3.5 μA/cm²), while retaining the inherent corrosion resistance and oxidation stability of boron-doped carbon. This study is the first to confirm the feasibility

of boron-doped carbon as a fuel cell electrocatalyst carrier, providing a new approach to reducing precious metal usage and enhancing electrode stability.

Meibuhr et al. [43] conducted a systematic study on the performance and mechanism of boron carbide (B4C) as a cathode catalyst in alkaline fuel cells. The study involved preparing porous nickel-based electrodes by mixing boron carbide with polytetrafluoroethylene (Teflon) and conducting polarization tests in a 45% KOH electrolyte. The experimental results showed that the boron carbide electrode exhibited stable oxygen reduction catalytic activity at a current density of 50 mA/cm², with its polarization behavior showing no significant correlation with the catalyst loading. However, after long-term operation, the performance of low-loading electrodes deteriorated more rapidly. After removing impurities via an acid/alkali cleaning process, the electrode polarization resistance decreased by approximately 30%, and performance remained stable during a 150-hour test, validating the critical role of impurity control in enhancing catalyst stability. Research indicates that boron carbide's high electrical conductivity (electron conductor), corrosion resistance, and resistance to electrochemical oxidation make it a potential low-cost cathode material. However, its catalytic activity remains lower than that of precious metal catalysts. Comprehensive analysis suggests that boron carbide is more suitable as a catalyst support material. By optimizing the surface properties and impurity content of the support, the long-term stability and economic viability of fuel cell cathodes can be significantly enhanced.

Mu et al. [44] prepared platinum-based catalysts (Pt-RGO/B4C) loaded with nano-boron carbide (B4C)-intercalated reduced graphene oxide (RGO) using the ethylene glycol reduction method, and investigated their performance and stability in the oxygen reduction reaction (ORR) of proton exchange membrane fuel cells (PEMFCs). The study demonstrated that B4C nanoceramic intercalation effectively suppresses graphene agglomeration and wrinkling, forming a highly ordered sandwich structure that enables uniform dispersion and full exposure of Pt nanoparticles, significantly enhancing the catalyst's electrochemical active surface area (ECSA) and mass activity. Experimental data show that the ECSA of Pt-RGO/B4C reaches 121 m²/g, representing a 55% and 92% increase compared to Pt/RGO (78 m^2/g) and commercial Pt/C (63 m^2/g), respectively (Figure 6-a). Its ORR mass activity is 185 A/gPt, which is 1.8 times that of Pt/RGO and 2.9 times that of Pt/C (Figure 6-b). After 10,000 accelerated durability tests, Pt-RGO/B4C retained 45.2% of its initial ECSA, significantly outperforming Pt/RGO (29.7%) and Pt/C (23.4%) (Figure 6-c). The team revealed that B4C intercalation restricts the migration and agglomeration of Pt nanoparticles through steric hindrance effects, enhances the conductivity and chemical stability of graphene, and significantly improves the catalyst's corrosion resistance and long-term stability.

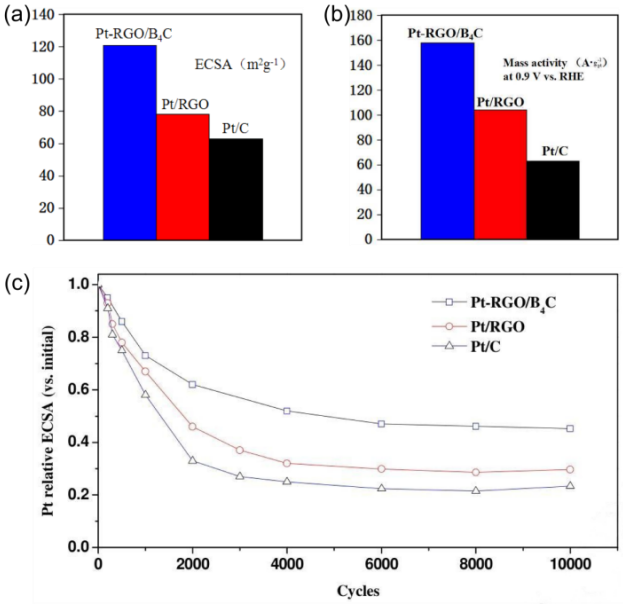

Figure 6 (a)ECSA of Pt-RGO/SiC, Pt/RGO and commercial Pt/C catalysts.(b)mass activities at +0.9 V vs. RHE in 0.1M HClO4 solution.(c)ECSA decay as a function of the number of potential cycles

4 Conclusions and Future Perspectives

4.1 Conclusions

This review establishes that boron carbide (B4C) and its composites exhibit significant potential in mitigating critical challenges across new energy battery systems, leveraging their structural rigidity, chemical robustness, tunable semiconductivity, and surface reactivity. Key advancements include:

In lithium-ion batteries (LIBs), B4C functions as a robust framework or interfacial buffer (e.g., Si/B4C/graphite systems), effectively constraining volume expansion in high-capacity anodes while enhancing electron/ion transport, thereby synergistically improving specific capacity and cyclability.

For sodium-ion batteries (SIBs), its three-dimensional architecture provides stabilized Na^+ diffusion pathways (e.g., VSe2/B4C@HCG), physically mitigating electrode pulverization.

In lithium-sulfur (Li-S) batteries, B4C chemically anchors polysulfides via B-S/C-S bonding and catalyzes their conversion (e.g., BC-NWs@ACT/S/rGO), substantially suppressing shuttle effects and reinforcing cathode integrity.

Within fuel cells, as a Pt-catalyst support (e.g., Pt-RGO/B4C), its corrosion resistance and surface properties optimize catalytic dispersion and oxygen reduction reaction stability.

Nevertheless, persistent challenges include high

nanomaterial synthesis costs, insufficient intrinsic ionic conductivity, and unresolved interfacial reaction mechanisms.

4.2 Future perspectives

To advance B4C composites in energy storage, four strategic research priorities are proposed:

(1) Performance Optimization: Elucidate structure-property relationships through integrated computational-experimental approaches to precisely engineer materials for enhanced ionic transport, volume-change accommodation, and polysulfide entrapment, ultimately boosting energy density, longevity, and safety.

(2) Process Innovation: Develop scalable, energy-efficient synthesis routes for nanostructured B4C (nanowires, nanosheets, porous architectures). Innovate one-step/in situ fabrication of composite electrodes to streamline manufacturing, reduce costs, and improve interfacial cohesion.

(3) Advanced Interface Engineering: Decipher interfacial interaction mechanisms to design novel modification strategies, thereby minimizing interfacial resistance, stabilizing electrode-electrolyte interfaces, and suppressing parasitic reactions during cycling.

(4) Cross-Disciplinary Integration: Foster convergence of materials science, electrochemistry, and characterization physics. Employ atomic-scale analytical techniques to unravel reaction mechanisms while adapting methodologies from adjacent fields to catalyze innovation in battery technology.

Use of AI tools declaration: The author declares that no artificial intelligence (AI) tools were used in the creation of this article.

Acknowledgments: This work was supported by the Science and Technology Program of Henan Province, China (No.222102230034), National College Student Innovation and Entrepreneurship Training Program (No.202510463011), the Characteristic Course Project of Integration of Specialty and Innovation of Henan University of Technology in 2024 (No. 2024ZCRH-10). We thank Lady L. P. Guo from the School of Foreign Languages at Henan University of Technology for help.

Conflict of interest: The author declares no conflict of interest.

References

[1] Boldin M S, Berendeev N N, Melekhin N V, et al. Review of ballistic performance of alumina: Comparison of alumina with silicon carbide and boron carbide [J]. Ceramics International, 2021, 47(18): 25201-25213.

[2] Gosset D. Absorber materials for Generation IV reactors [M] // Structural materials for generation IV nuclear reactors. Woodhead Publishing, 2017: 533-567.

[3] Sheikhi S, Stroberg W, Hogan J D. Effects of chain configuration and stoichiometry on the behavior of boron carbide from first-principle calculations [J]. Materials Today Communications, 2024, 40: 110205.

[4] Aselage T L. High temperature thermoelectric properties of boron carbide [J]. MRS Online Proceedings Library (OPL) , 1991, 234: 145.

[5] Domnich V, Reynaud S, Haber R A, et al. Boron Carbide: Structure, Properties, and Stability under Stress [J]. Journal of the American Ceramic Society, 2011, 94(11): 3605-3628.

[6] Song S, Xu W, Cao R, et al. B4C as a stable non-carbon-based oxygen electrode material for lithium-oxygen batteries [J]. Nano Energy, 2017, 33: 195-204.

[7] Wang H, Ma C, Yang X, et al. Fabrication of boron-doped carbon fibers by the decomposition of B4C and its excellent rate performance as an anode material for lithium-ion batteries [J]. Solid State Sciences, 2015, 41: 36-42.

[8] Duhduh A A, Saraswat S K, Lagum A A, et al. Exploring Ni-doped boron carbide nanotubes: Structural and electronic properties for proton-exchange membrane fuel cells [J]. Inorganic Chemistry Communications, 2023, 155: 111110.

[9] Pellegrini V, Bodoardo S, Brandell D, et al. Challenges and perspectives for new materials solutions in batteries [J]. Solid State Communications, 2019, 303: 113733.

[10] Goikolea E, Palomares V, Wang S, et al. Na-ion batteries-approaching old and new challenges [J]. Advanced Energy Materials, 2020, 10(44): 2002055.

[11] Thevenot F. Boron carbide-a comprehensive review [J]. Journal of the European Ceramic Society, 1990, 6(4): 205-225.

[12] Reddy K M, Liu P, Hirata A, et al. Atomic structure of amorphous shear bands in boron carbide [J]. Nature Communications, 2013, 4(1): 2483.

[13] Yang X , Goddard W A , An Q .The Structure and Properties of Boron-Very-Rich Boron Carbides: B12 Icosahedra Linked through Bent CBB Chains[J].The Journal of Physical Chemistry C, 2018, 122(4): 2448-2453.

[14] Mondal S. New insights into the bonding mechanism of boron carbide[J]. Acta Crystallographica Section A: Foundations and Advances, 2017, 73(a2):C382.

[15] Feng B, Martin H P, Michaelis A. Synthesis of Boron Carbide Powder via Rapid Carbothermal Reduction Using Boric Acid and Carbonizing Binder [J]. Ceramics, 2022, 5(4): 837-847.

[16] Eremeeva Z V , Myakisheva L V , Panov V S , et al.Spark Plasma Sintering of the Stock Material Made of the Boron Carbide Obtained by Different Methods[J].Inorganic Materials: Applied Research, 2019, 10(1): 74-80.

[17] Torabi O, Ebrahimi-Kahrizsangi R. Synthesis of B_4C, Al_2O_3, and AlB12 reinforced Al matrix nano composites via mechanochemical method[J]. Journal of Composite Materials, 2012, 46(18):2227-2237.

[18] Wei, Z. An overview of the synthesis of silicon carbide-boron carbide composite powders [J]. Nanotechnology Reviews, 2023, 12(1): 20220571.

[19] Avcıoğlu S, Buldu-Akturk M, Erdem E, et al. Boron carbide as an electrode material: Tailoring particle morphology to control capacitive behaviour [J]. Materials, 2023, 16(2): 861.

[20] Zhang L, Shi J, Shen C, et al. B4C-Al Composites Fabricated by the Powder Metallurgy Process[J].Applied Sciences, 2017, 7(10):1009.

[21] Wang X, Gao X, Zhang Z, et al. Advances in modifications and high-temperature applications of silicon carbide ceramic matrix composites in aerospace: A focused review[J]. Journal of the European Ceramic Society, 2021, 41(9): 4671-4688.

[22] Kuzubov A, Kuzubov, Aleksandr S, et al. High-capacity electrode material BC3 for lithium batteries proposed by ab initio simulations [J]. Physical Review B: Condensed Matter and Materials Physics, 2012, 85(19): 195415.

[23] Synthesis and Characterization of Li-containing Boron Carbide r-Li similar to 1B13C2 [J]. Zeitschrift fur Anorganische und Allgemeine Chemie, 2019, 645(3): 362-369.

[24] Chen X, Li X, Ding F, et al. Conductive Rigid Skeleton Supported Silicon as High-Performance Li-Ion Battery Anodes[J]. Nano Letters, 2012, 12(8):4124-4130.

[25] Su W, Xie Y, Wu K, et al. SnS2/B4C@OUCNTs as a high-performance anode material for lithium-ion batteries[J].Ionics, 2023 , 29: 3955-3969.

[26] Tan Y, Luo H, Zhang H, et al. Graphene nanoplatelet reinforced boron carbide composites with high electrical and thermal conductivity[J]. Journal of the European Ceramic Society, 2016, 36(11):2679-2687.

[27] Ding S, Yan X, Rehman J, et al. Revealing the key factors affecting the anode performance of metal-ion batteries: a case study of boron carbide monolayers[J]. Journal of Materials Chemistry A: Materials for Energy and Sustainability, 2024, 12(40):27703-27711.

[28] Hussain K, Muhammad I, Wu W, et al. 3D Porous Metallic Boron Carbide Crystal Structure with Excellent Ductility [J]. Advanced Theory and Simulations, 2021, 4(12): 2100325.

[29] Zhang H, Xiong D, Xie Y, et al. A simple synthesis of VSe_2/B_4C@HCG composite as high-performance anodes for sodium-ion batteries[J]. Journal of Alloys and Compounds, 2023, 935(Part2): 168111.

[30] Sun Y, Yang Y. Shi X L, et al. Self-standing and high-performance B4C/Sn/acetylene black@reduced graphene oxide films as sodium-ion half/full battery anodes [J]. Applied Materials Today, 2021, 24: 101137.

[31] Fang R, Chen K, Sun Z, et al. Realizing high-energy density for practical lithium-sulfur batteries [J]. Interdisciplinary Materials, 2023, 2(5): 761-770.

[32] Zhou G, Chen H, Cui Y. Formulating energy density for designing practical lithium-sulfur batteries [J]. Nature Energy, 2022, 7(4): 312-319.

[33] He J, Bhargav A, Manthiram A. High-energy-density, long-life lithium-sulfur batteries with practically necessary parameters enabled by low-cost Fe-Ni nanoalloy catalysts [J]. ACS Nano, 2021, 15(5): 8583-8591.

[34] Manthiram A, Fu Y, Su Y S. Challenges and prospects of lithium-sulfur batteries [J]. Accounts of Chemical Research, 2013, 46(5): 1125-1134.

[35] Manthiram A, Chung S H, Zu C. Lithium-sulfur batteries: progress and prospects [J]. Advanced Materials, 2015, 27(12): 1980-2006.

[36] Song N, Gao Z, Zhang Y, et al. B4C nanoskeleton enabled, flexible lithium-sulfur batteries [J]. Nano Energy, 2019, 58: 30-39.

[37] Luo L, Chung S H, Yaghoobnejad Asl H, et al. Long-Life Lithium-Sulfur Batteries with a Bifunctional Cathode Substrate Configured with Boron Carbide Nanowires[J]. Advanced Materials, 2018, 30(39): e1804149.

[38] Zhang R, Chi C, Wu M, et al. A long-life Li-S battery enabled by a cathode made of well-distributed B4C nanoparticles decorated activated cotton fibers [J]. Journal of Power Sources, 2020, 451: 227751.

[39] Lv H, Peng T, Wu P, et al. Nano-boron carbide supported platinum catalysts with much enhanced methanol oxidation activity and CO tolerance [J]. Journal of Materials Chemistry, 2012, 22(18): 9155-9160.

[40] Sharma A, Rangra V S, Thakur A. Synthesis, properties, and applications of MBenes (two-dimensional metal borides) as emerging 2D materials: a review [J]. Journal of Materials Science, 2022, 57(27): 12738-12751.

[41] Zhu G, Li G, Zhao X, et al. Application of diamond and super-hard carbide in fuel cell catalysis [J]. Ionics, 2023, 29(12): 4971-4986.

[42] Grubb W T, McKee D W. Boron carbide, a new substrate for fuel cell electrocatalysts [J]. Nature, 1966, 210(5032): 192-194.

[43] Meibuhr S G. Performance of oxygen fuel cell cathodes catalysed with boron carbide [J]. Nature, 1966, 210(5034): 409-410.

[44] Mu S, Chen X, Sun R, et al. Nano-size boron carbide intercalated graphene as high performance catalyst supports and electrodes for PEM fuel cells [J]. Carbon, 2016, 103: 449-456.

Viser Technology Pte. Ltd.
Research and Application of Materials Science
DOI: 10.33142/rams.v7i1.18642

Research Article Open Access

Comparison and Verification of the Potential Applicability of $BaTi_4O_9$ in the Field of Photocatalytic H_2 Evolution

Mengjie CUI[1], Imran MUHAMMADA[1], Tiezhen REN[1*], Xinwei YANG[2], Pengfei LIU[2], Xiaoming WU[2]

1. State Key Laboratory of Chemistry and Utilization of Carbon Based Energy Resources and Key Laboratory of Coal Clean Conversion & Chemical Engineering Process (Xinjiang Uyghur Autonomous Region), College of Chemical Engineering, Xinjiang University, Urumqi, Xinjiang 830046, China
2. Xinjiang Joinworld Company, Urumqi, Xinjiang, 830013, China

[*]***Corresponding Author:*** *Tiezhen REN, E-mail: rtz@xju.edu.cn*

Abstract

Photocatalytic hydrogen evolution is of great importance with the proceeding of dual carbon goals, for inorganic catalysts have been explored with high efficiency. The structure and properties of oxide composites might take advantage of each compound and display an increased activity. In our previous study, boron doped-$Cu_3Ni/BaTi_4O_9$ possessed a porous structure and its photocurrent response was apparent. To further verify its excellent catalytic activity, Al_2O_3, and SiO_2 were selected to replace with $BaTi_4O_9$ to prepare different composites. The physical and chemical features of each sample were characterized with SEM, XRD, XPS, etc. to reveal their structural variations. Correspondingly, the H_2 evolution rate was investigated with gas chromatography under the sunlight irritation. A distinct hydrogen yield was recorded with prepared samples. Further, the projected density of states analysis was taken through density functional theory calculations to appreciate the conduction band of the composite. The offered electrons during the photocatalytic process and the potential applicability of composites in the field of photocatalysis was verified.

Keywords: *Photocatalytic H_2 evolution; B doped $Cu_3Ni/BaTi_4O_9$; Porous structure; DFT calculation*

1 Introduction

Oxygenated materials are one of the most important catalysts, playing an irreplaceable role in various fields of photocatalysis, such as photocatalytic H_2 evolution, organic matter degradation, and CO_2 reduction. Various inorganic oxygen materials have attracted widespread attention and applied by researchers [1]. Such as $BaTi_4O_9$ (BTO) has a pentagonal prism tunnel structure and is a semiconductor with a bandgap of 3.57 eV for the potential value in the photocatalytic processes [2,3].

The cost effective Al_2O_3 has excellent chemical stability and high thermostability [4] making it widely used in photocatalysis [5,6]. A notable example of its utilization in the preparation of Pt and Al_2O_3 layers was simultaneously loaded onto TiO_2 nanoparticles to obtain an $Al_2O_3/TiO_2/Pt$ composite material [7]. Due to the presence of plentiful defect sites in Al_2O_3/TiO_2, Al_2O_3 also serves as an excellent electron acceptor for TiO_2. The transfer of photo-generated electrons from TiO_2 to the defect level of amorphous Al_2O_3 greatly facilitates the separation of charge carriers [8]. This machanism leads to the initial H_2 evolution rate increased from 0.4 μM min^{-1} on TiO_2/Pt to 0.9 μM min^{-1} on $Al_2O_3/TiO_2/Pt$. Therefore, introducing Al_2O_3 onto TiO_2 could significantly enhance catalytic activity to generate H_2. Moreover, Yanet et al. [9] prepared Al_2O_3:Ce^{3+}/Ce^{4+} materials by using the sol-gel method for the photodegradation of phenol. It was found that the degradation rate of phenol by Al_2O_3 material with 1.0 wt.% Ce could reach 94 % after 3 h of photocatalytic reaction.

Besides that, SiO_2 has the advantages of high heat resistance and high specific surface area, making it suitable as a catalyst in high temperature reactions. Therefore, it has also been applied in the field of photocatalysis. Experimental indicate that the composite material of TiO_2 and SiO_2 has high Ti^{3+} defects and oxygen vacancy. Through close contact of SiO_2/TiO_2 composite material with CaP to form a Z-type photocatalyst, the H_2 evolution rate could respectively reach 80.1 μmol g^{-1} and 94.0 μmol g^{-1} in pure seawater and artificial seawater within 4 h [11]. In addition, Wang et al. [10] successfully prepared ternary heterostructure catalysts $ZnIn_2S_4@SiO_2@TiO_2$ ($ZIS@SiO_2@TiO_2$) by simple sol-gel and solvothermal methods. Homogeneous mixing of TiO_2 and SiO_2 could form $SiO_2@TiO_2$

Received on March 10, 2025; Accepted on April 28, 2025

nanoparticles. Then the nanoparticles were uniformly inserted into the two-dimensional layered ZIS to form a ternary heterostructure, which effectively promotes the separation and transport of electrons (e^-) and holes (h^+). The 150%-ZIS@SiO_2@TiO_2 nanocomposites exhibited an excellent H_2 evolution rate (618.3 μmol g^{-1} h^{-1}) under visible light irradiation, and the Apparent Quantum Efficiency (AQE) at 380 nm could reach 17.56 %.

Several studies have substantiated the activity of Al_2O_3 and SiO_2 in the field of photocatalysis. In previous studies, our group discussed the modification of BTO with CuNi alloy and non-metallic element boron (B) for the photocatalytic H_2 evolution. To further verify the advantages of Cu_3Ni alloy and B on the activity of BTO and the potential of BTO in the photocatalysis field, alumina (Al_2O_3) and silicon oxide (SiO_2), were chosen to replace BTO in photocatalytic processes. The physical structures and photo-current of the prepared sample were investigated through the characterizations of the XRD, SEM, UV-vis, etc. The performance of H_2 evolution was revealed using gas chromatography. Following the hydrogen yield, the contributions of atomic states were investigated with the projected density of states analysis.

2 Experimental

2.1 Materials

All the reagents used in the experiment were of analytical grade without any further purification. $BaCO_3$, TiO_2, KCl, $BaCl_2$, and $Bi_4Ti_3O_{12}$ were brought from Sinopharm Chemical Reagent Co., Ltd, while AlOOH was provided by Xinjiang ZhongHe Co., Ltd. The rice husk (RH) and 30T/D electron-assisted thermal decomposition treatment equipment were provided by Harbin Dingdi Technology and Environmental Protection Co., Ltd. The Cupric Acetate Monohydrate ($Cu(CH_3COO)_2·H_2O$, 99.0 %), Nickel Acetate ($Ni(CH_3COO)_2·4H_2O$, 99.0 %), and Sodium Borohydride ($NaBH_4$, 98 %) were purchased from Tianjin Yongsheng Chemical Co., Ltd. Additionally, the triethanolamine (TEOA, 97 %) and C_3H_8O was purchased from Aladdin Reagent (Shanghai) Co., Ltd.

2.2 Preparation of BTO photocatalyst

BTO was synthesized using the molten salt method. The $BaCO_3$ and TiO_2 were mixed with molten salts (KCl and $BaCl_2$) and were milled for 8 h. Then, the slurries were mixed with the $Bi_4Ti_3O_{12}$ particles and ball-milled for 1 h. After drying, the reactants were heated at 1080 ℃ for 3 h. Then the powders were stirred in deionized water multiple times to remove salts, further put in a 2 mol L^{-1} of dilute nitric acid for 20 min to ensure that the oxides of Bi had reacted completely. Finally, the products were washed in deionized water several times to obtain pure BTO [11].

2.3 Preparation of Al_2O_3 photocatalyst

First, 1 g of AlOOH and 10 ml of C_3H_8O were mixed, and the mixture was respectively placed in a 70 ℃ constant temperature water bath for 8 h at 1500 R·min^{-1} high speed. Subsequently, , the mixture was transferred into a 100 ml autoclave with the Teflon lining for the hydrothermal reaction at a constant temperature of 200 ℃ for 24 h. Afterward, the substance was filtered and washed using deionized water and anhydrous alcohol. Then, the obtained products were dried for 30 min. The obtained precursor was respectively sintered at 600 ℃ for 2 h and the heating rate was 5 ^oC·min^{-1}. Finally, the white Al_2O_3 powder was collected.

2.4 Preparation of SiO_2 photocatalyst

The RH undergoes a simple sorting from the feeding port. It passes through a drying layer and is dried by hot gas at the bottom of the reaction device for 1 h. Next, enter the thermal decomposition layer. Here a stream of electron containing air (electrons injected into air) is fed into the device through the air inlet on the device wall by using a blower in the device center, which is helpful to increase the temperature of the hot zone. On the other hand, the radiation energy released by the ceramics, which was collected from the previous treatment, further reflects the reactor section and promotes the reactor temperature. After continuous treatment for 6 h, the furnace was shut down and the SiO_2 sample was collected.

2.5 Preparation of B(3)-Cu_3Ni/X photocatalyst

In brief, B(3)-Cu_3Ni/$Ba2Ti_4O_9$ was obtained with the following protocol. $Cu(CH_3COO)_2·H_2O$, $Ni(CH_3COO)_2·4H_2O$, and BTO were mixed with the mass ratio of 3:1:1 to get Cu_3Ni/$Ba_2Ti_4O_9$. In the mean time, 20 mL of 3%$NaBH_4$ was added and then with stirring till uniformly mixed at room temperature. Then the mixture was hydrothermal treated in an autoclave at 120 ^oC for 6 h. After cooling to room temperature, the precipitates were collected and washed with deionized water in sequence several times. Subsequently,, the solid sample was calcined at 600 ^oC for 2 h using N_2 as the carrier gas with a heating rate of 5 ^oC min^{-1} to obtain B(3)-Cu_3Ni/BTO. Correspondingly, B(3)-Cu_3Ni/Al_2O_3 and B(3)-Cu_3Ni/SiO_2 were prepared in same conditions.

2.6 Characterizations

To observe the morphology of the prepared samples, a scanning electron microscope (SEM) (Hitachi Electronics SU8010, Japan) was used. The structural information of the samples was characterized by the X-ray diffraction (XRD) using Bruker D8 Advance diffractometer (Bruker, Germany) with Cu-Kα radiation at 30 kV and 30 mA. The main functional groups of the sample were analyzed using the VERTEX 70 FTIR Spectrometer (Bruker Company,

Germany) using the KBr pellet method. To explore its photo response the UV-vis diffuse absorption spectra (Metash UV-8000, China) were used.

2.7 Photoelectrochemical tests

The photocurrent electrode was prepared as follows. 2 mg of the sample powder and 6 mL of ethanol were mixed with ultrasonic dispersion for 30 min. Then 100 μL of the suspension was uniformly dropped on the surface of prepared indium tin oxide (ITO) (2 cm × 2 cm) conductive glass. After the membrane was formed on the ITO substrate, it was cleaned with distilled water and ethanol in sequence for 1 h. Finally, the electrode was dried in an oven at 60 ℃ and an effective area of 4 cm^2 covered with the sample was successfully obtained.

The photocurrent response of samples was measured by the electrochemical workstation (Zahner ZENNIUM IM6) in a standard three-electrode system at room temperature. In the system, Ag/AgCl was the reference electrode and Pt/C acted as a counter electrode. The sodium sulfate solution (0.2 mol L^{-1}) was used as an electrolyte. The white light-emitting diode with the intensity of 10 mW·cm^2 was used as the light source, and the switching state of the light source was switched every 20 s [12].

The electrochemical measurements, including the electrochemical impedance test (EIS) and Mott-Schottky (M-S) test, were recorded with the electrochemical workstation. The electrolyte was set in 1 M of KOH solution.

2.8 Photocatalytic tests

In the photocatalytic H_2 evolution experiment, the 300W Xenon lamp, reaction device, and gas chromatography (Agilent 8860) were connected to calculate the H_2 evolution of photocatalysts. The 40 mg of photocatalyst and 8 mL of TEOA as the sacrificial agent were dispersed into a reaction apparatus containing 80 mL of pure water [13]. Simultaneously, cooling water was connected to maintain the photocatalytic process at approximately room temperature. The argon gas (Ar) was used as the carrier gas, and injected into the reactor for over 20 min to remove the air before illuminating.

After completing the blowing process, the actual H_2 evolution was tested by sampling with a GC analyzer at the 5th min of the initial reaction stage. Subsequently, sampling testing was conducted every 15 min for a total of 300 min, which is 5 h. Once the test was completed, the solid catalyst was dried in an 80 ^oC oven for 6 h through the centrifuge and washing steps, then the sample underwent 4 cycles of 5 h each to test its cyclic performance.

To calculate the AQE, we used a xenon lamp with various optical filters to obtain light with different wavelength ranges. It could be defined using an equation (1):

$$AQE = \frac{N_e}{N_p} \times 100\ \% = \frac{2n(H_2)}{N_p} = \frac{2n(H_2)(h \times c)}{I \times A \times \lambda} \times 100\ \% \quad (1)$$

In the above formula, $n(H_2)$ represents the number of H_2 molecules produced per second, I (W cm^{-2}) represents the energy of the light source per unit area, A (cm^2) represents the illuminated area, λ represents the wavelength of the incident light, h is the Planck constant, and c means the speed of light [14].

2.9 DFT calculations

The DFT was employed to investigate the electronic properties of B(3)-Cu_3Ni/BTO, B(3)-Cu_3Ni/Al_2O_3 and B(3)-Cu_3Ni/SiO_2 [15]. The system's properties are calculated by optimizing the corresponding model structure, including relaxing all atomic positions. The exchange correlation energy between electrons is described by the PBE (Perdew Burke Ernzerhof) functional under the generalized gradient approximation (GGA) [16,17], which is implemented in the CASTEP program of Device Studio [18]. A plane wave's cutoff energy is set to 300 eV, and the energy convergence standard is 2 × 10^{-5} eV per atom. The force on the relaxed atom is less than 0.02 eV $Å^{-1}$, and the Brillouin zone is sampled using a 4 × 4 × 1 grid. This method is used to calculate the density of states (DOS) of various catalysts. The highest energy level occupied by electrons is set to energy zero during the calculation process [19].

3 Results and Discussion

The microstructure of composites was observed through SEM. Figure 1a shows the BTO exhibits a dispersed and irregular nanosheet layered structure. Meanwhile, B(3)-Cu_3Ni/BTO photocatalyst displays an uneven porous surface with 1～2 μm macropores and a large number of abundant mesopores appearing (Figure 1b). The Al_2O_3 in Figure 1c exhibits agglomerated spherical nanoparticles with a particle size of approximately 30 nm [20,21]. However, the B(3)-Cu_3Ni/Al_2O_3 composite catalyst (Figure 1d) underwent significant changes, with the formation of 10 μm super large pits on the surface and formed unconnected hollow structures, which is not conducive to the transmission of electrons. This phenomenon might be due to the layering treatment of BTO, which makes it easier to form pores on the surface, while the agglomeration phenomenon of Al_2O_3 makes the surface more stable and more difficult to make pores. In Figure 1e represents irregularly large particles, with the agglomeration of crystalline grains, and the B(3)-Cu_3Ni/SiO_2 presents a rough surface with some agglomerated particles on it (Figure 1f).

The influence of different substances on the crystallinity was analyzed by XRD. As shown in Figure 2a, the diffraction peaks are located at 43.9 °, 53.1 °, and 75.1 °, corresponding to the (111), (200), and (220) crystal planes of Cu_3Ni alloy (JCPDS: 65-9048), respectively. The presence of (111) crystal plane corresponding to 43.93 ° is located between 45.38 ° of metal Ni (111) and 43.7 ° of metal Cu (111), indicating

the formation of Cu_3Ni alloy [22]. The main characteristic peaks at 23.26 °, 28.34 °, 30.11 °, 33.96 °, and 47.91 ° belong to the (301), (111), (211), (302), and (020) crystal planes of pure BTO (JCPDS: 77-1565)[23]. The characteristic peak corresponding to the (211) crystal plane of BTO in B(3)-Cu_3Ni/BTO tends to weaken. This might be due to the substitution of Ti or O in BTO by B atoms, which introduces defects changes the lattice parameters, and leads to structural intensity decreases [24]. This result indicates that B has been successfully doped into the BTO structure. The XRD peaks of Al_2O_3 (JCPDS: 29-0063) include the main peak at 37.36 °, 46.42 °, and 66.83 ° correspond to the (113), (004), and (044) crystal planes [25,26]. The characteristic peak of B(3)-Cu_3Ni/Al_2O_3 is mainly CuNi alloy, which may be due to the contribution of Al_2O_3 nanostructure. It is observed that the crystal structure of SiO_2 has strong characteristic peaks, which are consistent with cristobalite (JCPDS: 77-1317) and tridymite (JCPDS: 86-0681) [27]. Due to similar preparation conditions of these two crystal phases, when the crystallization temperature is below 1400 ℃, a cristobalite-tridymite (CT) structure will be formed [28]. The characteristic peaks of SiO_2 and CuNi alloy are both obvious in B(3)-Cu_3Ni/SiO_2. From the XRD results, it was observed that there are characteristic peaks of CuNi alloy in all three composites, and the characteristic peaks of BTO, Al_2O_3, and SiO_2 are also retained according to their relative strength as shown in Figure 2a. Notably, the strong characteristic peaks undergo slight shifts, which also proves that B replaces Ti, Al, and Si respectively, and connects with O to enter the BTO, Al_2O_3, and SiO_2.

The functional groups and chemical types of the catalyst was determined through FTIR analysis as depicted in (Figure 2b). Characteristic peak at approximately 621 cm^{-1} corresponds to the Ti-O stretching vibration of octahedral groups in complex perovskite structures, and the peak at 827 cm^{-1} displays the O-Ti-O stretching vibration, these characteristic peaks confirmed the presence of BTO [29]. The peaks at approximately 1655 ～ 1630 and 3400 ～ 3480 cm^{-1} correspond to the adsorbed water in the catalyst and the -OH on the surface [30,31]. The strong broadening band at 1000～400 cm^{-1} and two distinct peak bands indicate Al-O vibration [32]. Peaks around 1406 cm^{-1} and 1640 cm^{-1} are the bending vibration peaks of Al-OH [33], and several inconspicuous peaks in the broad peaks at low wavelengths, located at 1064 cm^{-1} and 746 cm^{-1}, respectively, representing the torsional and stretching vibrations of the Al-O bond [34,35]. SiO_2 shows peaks at 475 ～ 440 cm^{-1} and 870 ～ 805 cm^{-1}, represented by Si-O symmetric bending vibration and symmetric stretching [36]. Due to intermolecular dehydration, Si-O bonds polymerize to form Si-O-Si chains, which further indicates the presence of SiO_2 in the sample. The strong and wide peak is located in the region of 1100-1000 cm^{-1}, which is the transverse symmetric stretching vibration absorption peak of the Si-O-Si bond [37]. As the temperature of thermal decomposition increases, the characteristic peak here becomes sharper and smoother, indicating an increase in the purity of SiO_2 in the sample. Additionally, the peak near 1655～1630 cm^{-1} is the H-O-H bending vibration peak of water, which is a typical characteristic peak of white carbon black [38].

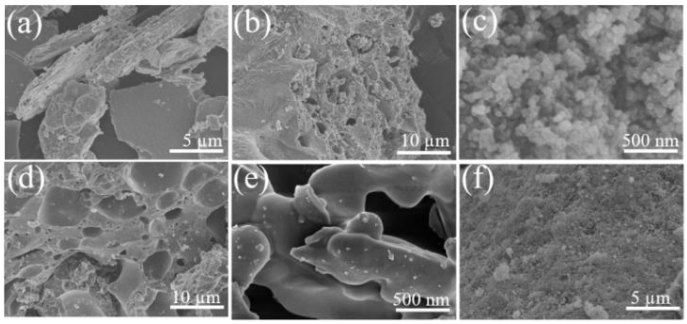

Figure 1 The SEM of (a) BTO, (b) B(3)-Cu_3Ni/BTO, (c) Al_2O_3, (d) B(3)-Cu_3Ni/Al_2O_3, (e) SiO_2 and (f) B(3)-Cu_3Ni/SiO_2

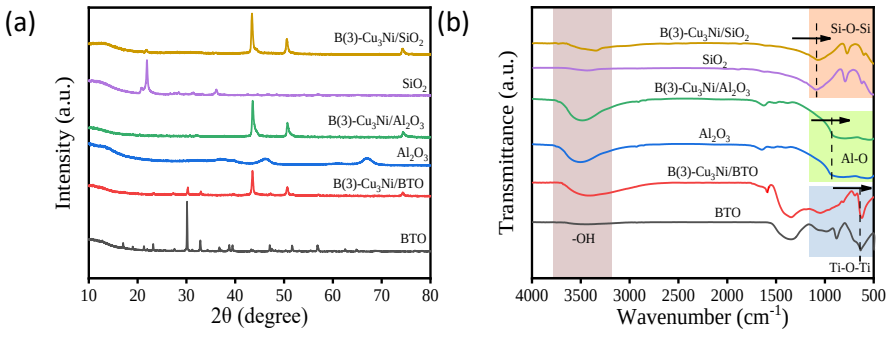

Figure 2 The (a) XRD spectra and (b) FTIR spectra of BTO, B(3)-Cu_3Ni/BTO, Al_2O_3, B(3)-Cu_3Ni/Al_2O_3, SiO_2 and B(3)-Cu_3Ni/SiO_2

With the doping of Cu_3Ni alloy, the intensity of the -OH peak at 3423 cm^{-1} significantly increases, indicating that Cu_3Ni could make the composite material more hydrophilic, which is conducive to the occurrence of photocatalytic water splitting reaction [39,40]. The comparison of the three composites shows that the Cu_3Ni alloy has a more significant effect on the surface functional groups of BTO. However, the vibration band of Cu_3Ni alloy in the complex is not detected because it is not active in FTIR and is not suitable for its detection [41]. Nevertheless, the characteristic peaks of the complex are consistent with their corresponding substances. Meanwhile, Due to the doping of B, the electronic structure of BTO, Al_2O_3, and SiO_2 have changed, resulting in the characteristic peaks of these substances all having a slight shift.

The photocatalytic activity is closely related to the light absorption performance of the photocatalyst. To explore the differences in optical properties between different oxides and corresponding composites, UV-vis tests were conducted (Figure 3a). The BTO has a lower absorption intensity in 410 ～ 1000 nm, with an absorption edge is around 410 nm. Al_2O_3 overall absorbance is the least, while SiO_2 exhibits superior absorbance in the visible light region, with an absorption edge is around 470 nm. It could be found that the light absorption ability of all three composites is significantly improved by modification with CuNi alloy and B, and the absorbance of B(3)-Cu_3Ni/BTO is the best.

To investigate the reason for photocatalytic activity increasing after B-doping, photoelectrochemical tests were conducted. In Figure 3b, all prepared photocatalysts exhibit repeatable photocurrent responses within each illumination cycle. During the switch light irradiation cycle, the photocurrent rapidly decreases in the dark. The photoelectric current response of composites is superior to that of pure oxides. B(3)-Cu_3Ni/BTO composite exhibits the highest photoelectric current response under visible light, followed by B(3)-Cu_3Ni/SiO_2, and finally B(3)-Cu_3Ni/Al_2O_3. This finding indicates that Cu_3Ni alloy and B greatly promote photocatalytic reactions making the composite have better separation efficiency for e^- and h^+ than pure oxides [42].

Then, an EIS test was conducted to clarify the charge transfer process at the interface between photocatalysts and electrolytes. The semicircle width in the high-frequency region reflects the charge transfer resistance (R_{ct}) [40]. In Figure 3c, the BTO has the smallest semi-circular diameter in the oxide, indicating that the charge at its interface is easily transferred to the surface to participate in the reaction[43]. The semicircles of all composites are smaller than their related oxides, meaning that the charge transfer resistance of the oxides after the composite of Cu_3Ni alloy and B is smaller, which is more conducive to the photocatalytic process. Among the composites, the semicircle diameter of the B(3)-Cu_3Ni/BTO is the smallest.

Meanwhile, the M-S curve generally describes the semiconductor properties of catalysts. A positive slope means an *n*-type semiconductor with e^- as carriers, while a negative slope means a *p*-type semiconductor with h^+ as carriers. From Figure 3d, both the oxide and its corresponding composites are *n*-type semiconductors with significant photocurrent response properties. As indicated the modification of Cu_3Ni and B do not alter the semiconductor properties of the catalyst. Comparing the test curves of all photocatalysts, the overall M-S curve of the composite material shows a significant increase, indicating an increase in free e^- in the catalyst after modification [44]. Especially, the slope of B(3)-Cu_3Ni/BTO is smaller than that of other catalysts, fitting to a faster rate of photogenerated charge transfer.

From the above tests, it could be found that the photoelectric characteristic pattern is BTO ＞ SiO_2 ＞ Al_2O_3. These correspond to the same sequence of the composites in the photocatalytic H_2 evolution reaction.

The effect of catalysts on the photocatalytic H_2 production process was investigated under a 300 W Xe lamp irradiation within 5 h, as shown in Figure 4a. BTO has the lower H_2 evolution, with only 9.11 μmol g^{-1} within 5 h. However, Al_2O_3 and SiO_2 do not produce H_2. During the first 30 min of the reaction, B(3)-Cu_3Ni/BTO has the highest H_2 evolution and could reach 1590.3 μmol g^{-1}. At the 300th min, the catalyst still participates in the reaction and produces H_2. However, the B(3)-Cu_3Ni/SiO_2 shows little H_2 evolution after 200 min, while B(3)-Cu_3Ni/Al_2O_3 showed little H_2 evolution after 150 min, resulting in the worst photocatalytic activity and stability.

Figure 4b shows the H_2 evolution rate of different oxides and corresponding composites. The maximum H_2 evolution rate of B(3)-Cu_3Ni/BTO is 318.06 μmol g^{-1} h^{-1}, is 101.18 times that of BTO (1.82 μmol g^{-1} h^{-1}), 6.69 times that of B(3)-Cu_3Ni/Al_2O_3 (47.57 μmol g^{-1} h^{-1}), and 3.61 times that of B(3)-Cu_3Ni/SiO_2 (88.12 μmol g^{-1} h^{-1}). The AQE of B(3)-Cu_3Ni/BTO, B(3)-Cu_3Ni/Al_2O_3, and B(3)-Cu_3Ni/SiO_2 samples were conducted. As shown in Figure 4c, the AQE matched well with the absorption spectrum. Moreover, the AQE of B(3)-Cu_3Ni/BTO is 8.91 % under the wavelength of 420 nm, which is significantly attributed to B(3)-Cu_3Ni/Al_2O_3 (1.33 %) and B(3)-Cu_3Ni/SiO_2 (2.47 %). The performance of the designed material was compared with previously reported work. It was observed that the prepared catalyst has a good hydrogen evolution rate, which can be attributed to its high surface porosity. Besides this, the prepared material water hydrogen evolution performance exhibits excellent cycling reactivity. After 4 cycles of experiments, Cu_3Ni/BTO the crystal structure of the catalyst has not changed, indicating that the catalyst has excellent cyclability [41], and the contaminant degradation reached up to 94% as compared to the previously reported literature [35]. Thus Cu_3Ni is suitable for BTO the composite ratio which will significantly improve the photocatalytic hydrogen production activity of the catalyst.

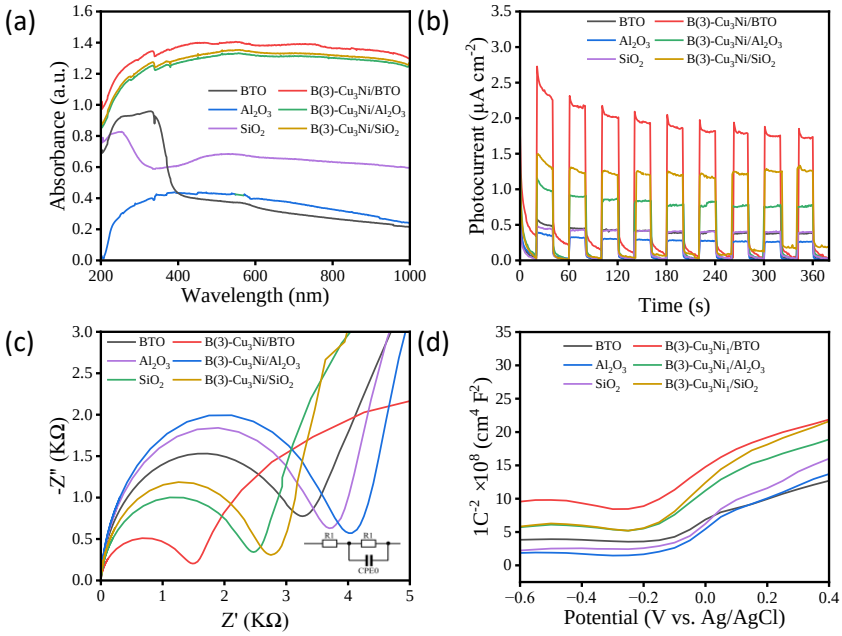

Figure 3 The (a) UV-vis absorbance spectra, (b) transient photocurrent density responses, (c) EIS spectroscopy, and (d) M-S spectroscopy of BTO, B(3)-Cu_3Ni/BTO, Al_2O_3, B(3)-Cu_3Ni/Al_2O_3, SiO_2 and B(3)-Cu_3Ni/SiO_2

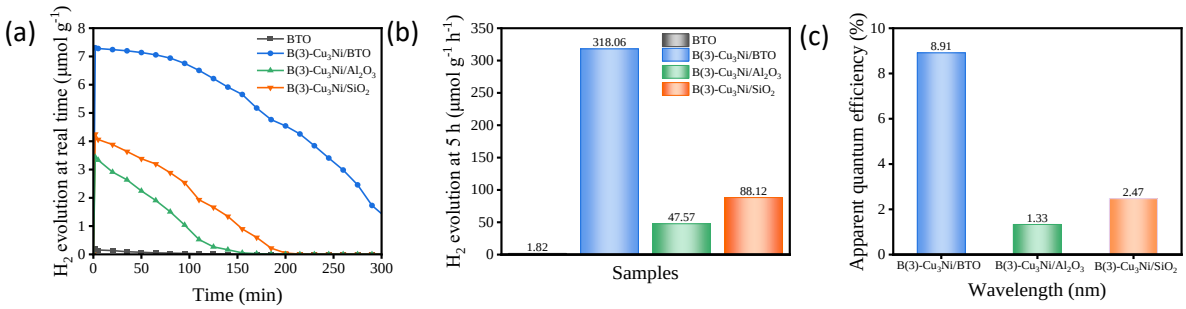

Figure 4 The real time photocatalytic H_2 evolution over time within 5 h under visible light irradiation (λ＞ 400 nm), and (b) H_2 evolution rate of BTO, B(3)-Cu_3Ni/BTO, B(3)-Cu_3Ni/Al_2O_3 and B(3)-Cu_3Ni/SiO_2; (c) The AQE value under 420 nm.

Based on the above performance testing results, it is elaborated that the H_2 evolution performance of the catalyst is consistent with the photoelectric characteristics, proving that BTO is more suitable for photocatalytic reaction processes. Different oxides not only affect the microstructure of the composite material but also alter its photocatalytic activity.

Combining the above analysis, the three different crystal structures were constructed by doping BTO, Al_2O_3, and SiO_2 with 3% B, separately. And the cell structures of composites are established by putting Cu_3Ni and oxides doped with B in the same space for DFT calculations. To compare the contributions of atomic states, Figure 5a shows the DOS and PDOS of the main atoms of B(3)-Cu_3Ni/BTO. The valence band (VB) of B(3)-Cu_3Ni/BTO is mainly composed of O 2p, while CB is composed of Ti 3d, Cu 2p, and Ni 2p, proving that after the composite of Cu_3Ni alloy and B(3)-BTO, CuNi alloy does indeed provide more free e^- for the CB of BTO to participate in the photocatalytic reaction. From Figure 5b, the VB of B(3)-Cu_3Ni/Al_2O_3 is mainly composed of Al 2p and O 2p, while CB is composed of Al 2p, with smaller contributions from other atoms. Compared with Figure 5a, the VB component in B(3)-Cu_3Ni/Al_2O_3 is composed of O 2p and Al 2p state cross-linking, indicating that the doping of 3% B has minimal effect on the electronic structure of Al_2O_3, and the minimum amount of e^- on the B(3)-Cu_3Ni/Al_2O_3 surface indicates that its catalytic activity is the lowest. In Figure 5c, the VB of B(3)-Cu_3Ni/SiO_2 is mainly composed of O 2p, while CB is composed of Si 2p and Cu 2p, with smaller contributions from other atoms. Moreover, the Si atom in B(3)-Cu_3Ni/SiO_2 provides a lower amount of e^- in CB, resulting in lower photocatalytic activity. The results obtained from DFT calculations are consistent with the experimental results, which also proves the accuracy of the experimental results.

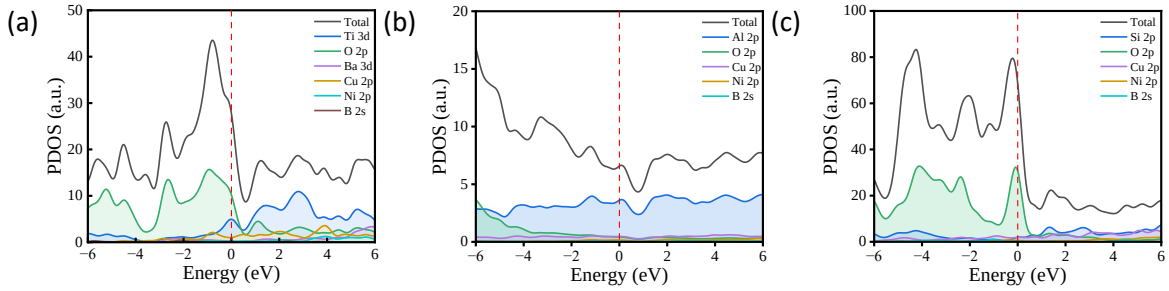

Figure 5 The DOS and PDOS plots for (a) B(3)-Cu_3Ni/BTO, (b) B(3)-Cu_3Ni/Al_2O_3, and (c) B(3)-Cu_3Ni/SiO_2. The black solid line represents the DOS rest of the color present PDOS in Figure 5a-c

4 Conclusions

The photocatalysis of hydrogen with B atoms doping in CuNi/BTO composite was discussed in the current research work. The conventional photocatalytic oxides (Al_2O_3 and SiO_2) were used to compare with BTO to explore the efficacy of BTO. Three different composites namely B(3)-Cu_3Ni/BTO, B(3)-Cu_3Ni/Al_2O_3, and B(3)-Cu_3Ni/SiO_2 were systematically investigated to demonstrate the advantages of BTO for photocatalysis. Notabley when, compared with Al_2O_3 nanoparticles and porous silicate, the BTO composite showed a high photo-current response and small resistance. Specifically, the B(3)-Cu_3Ni/BTO composite possessed a porous structure and exhibited superior optoelectronic properties and photocatalytic H_2 activity (318.06 μmol g^{-1} h^{-1}) than the corresponding nanoparticles. Moreover, the PDOS tests also proved that B(3)-Cu_3Ni/BTO could provide more e^- to participate in the redox reaction of photocatalytic reactions. The current finding demonstrates the practical significance, show casing the superior H_2 evolution rate of B(3)-Cu_3Ni/BTO (318.06 μmol g^{-1} h^{-1}). This result confirms the potential applicability of BTO in the field of photocatalysis and paves the way for the generation of high efficient material.

Acknowledgments: This work was supported by the Natural Science Foundation of Xinjiang Uygur Autonomous Region (2021D01A03), Key Research and Development Projects of Xinjiang Uygur Autonomous Region (2022B02038), Special Training Program for Scientific and Technological Talents of Ethnic Minorities in Xinjiang Uygur Autonomous Region (2020D03025), and Project of Tian chi talent leader in Xinjiang Uygur Autonomous Region (2022).

Reference

[1] W. M. ZHOU Shijie, REN Zhen, YANG Yusen, Preparation and application of metal oxides with various morphology for industrial catalysis [J]. CIESC Journal,2021(76):2972-3001.

[2] S. Ogura, K. Sato, and Y. Inoue, Effects of RuO_2 dispersion on photocatalytic activity for water decomposition of $BaTi_4O_9$ with a pentagonal prism tunnel and $K_2Ti_4O_9$ with a zigzag layer structure [J]. Physical Chemistry Chemical Physics, 2000(2):2449-2454.

[3] Y. Yamashita, K. Yoshida, M. Kakihana, et al. Polymerizable Complex Synthesis of $RuO_2/BaTi_4O_9$ Photocatalysts at Reduced Temperatures: Factors Affecting the Photocatalytic Activity for Decomposition of Water [J]. Chemistry of Materials,1999(11):61-66.

[4] M. Shekhar, J. Wang, W.-S. Lee, et al. Size and Support Effects for the Water-Gas Shift Catalysis over Gold Nanoparticles Supported on Model Al_2O_3 and TiO_2 [J]. Journal of the American Chemical Society, 2012(134):4700-4708.

[5] F. Li, Y. Zhao, Y. Liu, et al. Solution combustion synthesis and visible light-induced photocatalytic activity of mixed amorphous and crystalline $MgAl_2O_4$ nanopowders [J]. Chemical Engineering Journal, 2011(173):750–759.

[6] A. Zarubica, R. Ljupković, J. Papan, et al. Visible-light-responsive Al_2O_3 powder: Photocatalytic study. Optical Materials [J]. 2020(106):110013.

[7] W. Kim, T. Tachikawa, T. Majima, et al. Photocatalysis of Dye-Sensitized TiO_2 Nanoparticles with Thin Overcoat of Al_2O_3 : Enhanced Activity for H_2 Production and Dechlorination of CCl_4. The Journal of Physical Chemistry C [J]. 2009(113):10603–10609.

[8] F. Li, Y. Zhao, Y. Hao, et al. N-doped P25 TiO_2-amorphous Al_2O_3 composites: One-step solution combustion preparation and enhanced visible-light photocatalytic activity [J]. Journal of Hazardous Materials, 2012(239-240):118–127.

[9] Y. Piña-Pérez, F. Tzompantzi-Morales, R. Pérez-Hernández, et al. Photocatalytic activity of Al_2O_3 improved by the addition of Ce^{3+}/Ce^{4+} synthesized by the sol-gel method [J]. Photodegradation of phenolic compounds using UV light Fuel, 2017(198):11–21.

[10] L. Wang, H. Zhou, H. Zhang, et al. SiO_2 @TiO_2 Core@Shell Nanoparticles Deposited on 2D-Layered ZnIn2S4 to Form a Ternary Heterostructure for Simultaneous Photocatalytic Hydrogen Production and Organic Pollutant Degradation [J]. Inorganic Chemistry, 2020(59):2278–2287.

[11] L. Jin, Y. Huang, L. Zhang, et al. Formation mechanism of barium titanate single crystalline microplates based on topochemical transformation using bismuth-based

precursors [J]. Ceramics International, 2021(47):4543-4550.
[12] A. M. Hyde, S. L. Zultanski, J. H. Waldman, et al. General Principles and Strategies for Salting-Out Informed by the Hofmeister Series [J]. Organic Process Research & Development, 2017(21):1355-1370.
[13] S. Chen, J. Liao, Z. Zhou, et al. Boosting photocatalytic hydrogen evolution using a noble-metal-free co-catalyst: CuNi@C with oxygen-containing functional groups [J]. Applied Catalysis B: Environmental, 2021(291):120139.
[14] Z. Jiang, X. Xu, Y. Ma, et al. Filling metal-organic framework mesopores with TiO_2 for CO_2 photoreduction [J]. Nature, 2020(586):549–554.
[15] D. L. Chen Jingliang, Luan Lijun, Zhang Ru, et al. First-principles Calculation of Type-II C2N/ZnO Heterojunction as a Water Splitting Photocatalyst [J]. Materials Reports, 2023(37):21110258.
[16] W. Navarra, I. Ritacco, O. Sacco, et al. Density Functional Theory Study and Photocatalytic Activity of ZnO/N-Doped TiO_2 Heterojunctions [J]. The Journal of Physical Chemistry C, 2022(126):7000–7011.
[17] X. Tang, Q. Xue, X. Qi, et al. DFT and experimental study on visible-light driven photocatalysis of rare-earth-doped TiO_2 [J]. Vacuum, 2022(200):110972.
[18] M. Huang, Z. Zheng, Z. Dai, et al. DASP: Defect and Dopant ab-initio Simulation Package [J]. Journal of Semiconductors, 2022(43):042101.
[19] P. Ganguly, S. K. R., M. Muscetta, et al. New insights into the efficient charge transfer of ternary chalcogenides composites of TiO_2 [J]. Applied Catalysis B: Environmental, 2021(282):119612.
[20] Z. Gholizadeh, M. Aliannezhadi, M. Ghominejad, et al. High specific surface area γ-Al_2O_3 nanoparticles synthesized by facile and low-cost co-precipitation method [J]. Scientific Reports, 2023(13):6131.
[21] T.-P. Teng, Y.-H. Hung, T.-C. Teng, et al. Performance evaluation on an air-cooled heat exchanger for alumina nanofluid under laminar flow [J]. Nanoscale Research Letters, 2011(6):488.
[22] Z. Zhou, M. Wei, G. Yang, et al. Photoinduced electron-rich CuNi@C/TiO_2 catalyst for highly efficient hydrogen production from formaldehyde aqueous solution [J]. Journal of Alloys and Compounds, 2023(936):168360.
[23] X. Zhang, S. Tang, R. Li, et al. Synthesis and photocatalytic property of $BaTi_4O_9/RuO_2$ nanocomposites [J]. Materials Research Bulletin, 2013(48):609–612.
[24] A. N. Oliveros, J. A. I. Pimentel, M. D. G. de Luna, et al. Visible-light photocatalytic diclofenac removal by tunable vanadium pentoxide/boron-doped graphitic carbon nitride composite [J]. Chemical Engineering Journal, 2021(403):126213.
[25] G. Liu, J. Jiang, X. Wang, et al. Al_2O_3 nanoparticles modified the FeS_2 cathode to boost the interface wettability and electrochemical performance for thermal batteries [J]. Materials Letters, 2023(330):133290.
[26] L. Zhu, S. Pu, K. Liu, et al. Preparation and characterizations of porous γ-Al_2O_3 nanoparticles [J]. Materials Letters, 2012(83):73–75.
[27] I. M. Joni, L. Nulhakim, M. Vanitha, et al. Characteristics of crystalline silica (SiO_2) particles prepared by simple solution method using sodium silicate (Na_2SiO_3) precursor [J]. Journal of Physics: Conference Series, 2018(1080):012006.
[28] I. K. Moroz, G. N. Maslennikova, A. F. Mironova, et al. Formation of tridymite and cristobalite from quartz in porcelain [J]. Glass and Ceramics, 1980(37):147-150.
[29] A. Ali, S. Uddin, M. Lal, et al. Structural, optical and microwave dielectric properties of $Ba(Ti^{1-}xSnx)_4O_9$, $0 \le x \le 0.7$ ceramics [J]. Scientific Reports, 2021(11):17889.
[30] Z. Yan, K. Yin, M. Xu, et al. Photocatalysis for synergistic water remediation and H_2 production: A review [J]. Chemical Engineering Journal, 2023(472):145066.
[31] M. Ashour, I. Soliman, M. Mabrouk, et al. Silica Nanoparticles as a Potential Carrier for Doxycycline Hyclate [J]. Egyptian Journal of Biomedical Engineering and Biophysics, 2020(1034):40105.
[32] A. S. Jbara, Z. Othaman, A. A. Ati, et al. Characterization of γ- Al_2O_3 nanopowders synthesized by Co-precipitation method [J]. Materials Chemistry and Physics, 2017(188):24-29.
[33] S. Ponmudi, R. Sivakumar, C. Sanjeeviraja, et al. Influences of sputtering power and annealing temperature on the structural and optical properties of Al_2O_3:CuO thin films fabricated by radio frequency magnetron sputtering technique [J]. Journal of Materials Science: Materials in Electronics, 2019(30):18315-18327.
[34] A. Bazyari, Y. Mortazavi, A. A. Khodadadi, et al. Effects of alumina phases as nickel supports on deep reactive adsorption of (4,6-dimethyl) dibenzothiophene: Comparison between γ, δ, and θ-alumina [J]. Applied Catalysis B: Environmental, 2016(180):312-323.
[35] K. Atrak, A. Ramazani, and S. Taghavi Fardood, Green synthesis of amorphous and gamma aluminum oxide nanoparticles by tragacanth gel and comparison of their photocatalytic activity for the degradation of organic dyesalumina [J]. Journal of Materials Science: Materials in Electronics, 2018(29):8347–8353.
[36] L. Usgodaarachchi, C. Thambiliyagodage, R. Wijesekera, et al. Synthesis of mesoporous silica nanoparticles derived from rice husk and surface-controlled amine functionalization for efficient adsorption of methylene blue from aqueous solution [J]. Current Research in Green and Sustainable Chemistry, 2021(4):100116.
[37] M. M. Khayyat, G. K. Banini, D. G. Hasko, et al. Raman microscopy investigations of structural phase transformations in crystalline and amorphous silicon due to indentation with a Vickers diamond at room temperature and at 77 K [J]. Journal of Physics D: Applied Physics, 2003(36):1300–1307.
[38] M. Li, H. Shen, L. Zhuang, et al, SiO_2 Antireflection Coatings Fabricated by Electron-Beam Evaporation for Black Monocrystalline Silicon Solar Cells [J]. International Journal of Photoenergy, 2014(2014):1–5.
[39] J. Zhang, Y. Cao, F. Chen, et al. Tailoring hydrophilicity and electronic interactions and transfer: Enhancing hydrogen

production through size-tuned CuNi alloys [J]. Fuel, 2024(366):131364.
[40] R. Fang, Z. Yang, Z. Wang, et al. Transition metal tuned g-C_3N_4 induce highly efficient photocatalytic of ammonia borane to hydrogen evolution and mechanism investigation [J]. Fuel, 2023(334):126707.
[41] P. Zhang, G. Zeng, T. Song, et al. Synthesis of a plasmonic CuNi bimetal modified with carbon quantum dots as a non-semiconductor-driven photocatalyst for effective water splitting [J]. Journal of Catalysis, 2019(369):267–275.
[42] J. Li, Y. Huang, B. Luo, et al. Efficient photothermal-assisted photocatalytic hydrogen production over a plasmonic CuNi bimetal cocatalyst [J]. Journal of Colloid and Interface Science, 2022(626):975–984.
[43] T.-Z. Ren, M.-J. Cui, Y.-M. Zhao, et al. The Activated Carbon with Pyrolle-N from Cotton Stalk for the Electrochemical Performance [J]. Advanced Materials Science and Technology, 2022(4):79–92.
[44] T. Kou, M. Chen, F. Wu, et al. Carbon doping switching on the hydrogen adsorption activity of NiO for hydrogen evolution reaction [J]. Nature Communications, 2020(11):590.

Viser Technology Pte. Ltd.
Research and Application of Materials Science
DOI: 10.33142/rams.v7i1.18643

Research Article Open Access

Carbonized Polymer Dots as Electrolyte Additives to Inhibit Zinc Anode Corrosion and Enhance Full Cell Cycle Life

Qimeng ZHANG, Haizhu SUN*

Key Laboratory of Sustained and Advanced Functional Materials, College of Chemistry, Northeast Normal University, Changchun, Jilin, 130024, China

***Corresponding Author:** *Haizhu SUN*, *E-mail: sunhz335@nenu.edu.cn*

Abstract

Carbonized polymer dots(CPDs), as a new type of carbon-based nanomaterials, have been widely used in the fields of biosensing[1], light-emitting devices[2], and energy storage systems[3-4]due to their tunable photovoltaic properties and abundant surface functional groups. Especially in energy storage, it has good prospects and applications as an artificial negative electrode protective layer[5] for zinc-ion batteries(AZIBs). However, less research has been done on its use as an additive in zinc ion battery electrolyte[6]. We developed a method for the rapid synthesis of CPDs using citric acid as a substrate and urea as a nitrogen-doped additive using the microwave method at 1000W. The synthesized CPDs have graphitized carbon core centers as well as a wide range of peripheral functional groups. Due to the great potential of CPDs in the field of zinc ion batteries, we applied them as electrolyte additives in the electrolyte of aqueous zinc ion batteries, which can effectively inhibit the growth of dendrites on zinc anode, the precipitation of hydrogen and oxygen in the electrolyte, and at the same time, the corrosion current of the electrolyte on the anode is extremely low, which can greatly inhibit the corrosion of zinc anode in the electrolyte, and can effectively promote the rapid diffusion of zinc ions from the two-dimensional to the three-dimensional, which can greatly improve the long-cycle stability of zinc ion battery, as well as the stability of the long-cycle stability of the zinc ion battery. It can also effectively promote the rapid diffusion of zinc ions from two-dimensional to three-dimensional, which greatly improves the long cycle stability of zinc ion battery and the cycle life of the whole battery. The zinc iodine battery has a stable cycle time of 43,000 cycles, a capacity retention rate of 90%, and a Coulombic efficiency of 100%.

Keywords: *CPDs; microwave method; dendrite growth; corrosion; cyclic stability*

1 Introduction

In recent years, with the transition of global energy structure to renewable energy, large-scale energy storage technology has become the key to solve the stability of intermittent energy sources. However, the current mainstream lithium-ion batteries have hindered their marketability in the energy storage industry due to potential problems such as high cost, resource depletion and flammability of organic electrolyte[7-8]. Therefore, the development of secondary batteries with the advantages of safety, high efficiency, environmental protection and low cost has gradually become a trend[9]. The aqueous zinc ion battery has become a highly promising energy storage device due to its unique advantages. Zinc ion adopts non-flammable aqueous electrolyte, which fundamentally solves the risk of thermal runaway; zinc resources are abundant and inexpensive, which significantly reduces the cost of raw materials; at the same time, zinc is non-toxic, easy to recycle, and has better environmental compatibility. In addition, zinc anode has high theoretical specific capacity (820 mAh g^{-1}) and low electrochemical potential (-0.76 V)[10], with manganese-based, vanadium-based anode materials can realize efficient energy storage and fast charge and discharge. However, at the same time, zinc ion batteries also face certain problems, for example, the surface of zinc negative electrode is prone to tip effect due to the uneven distribution of electric field, forming dendritic crystal growth, piercing the diaphragm and causing short circuit, and hydrogen precipitation and chemical corrosion inevitably occurs in the aqueous electrolyte, which greatly reduces the cycling stability and coulombic efficiency of zinc ion batteries[11]. Therefore, based on the defects of zinc ion batteries, the use of microwave method to prepare citric acid, urea carbon point, as an electrolyte additive, not only can effectively inhibit the zinc negative electrode dendrite growth, electrolyte hydrogen precipitation and oxygen precipitation reaction, but also can improve the transmission efficiency of Zn^{2+}, and greatly improve the zinc ion batteries long-cycle stability, and the performance of the whole battery.

Received on March 9, 2025; Accepted on April 24, 2025

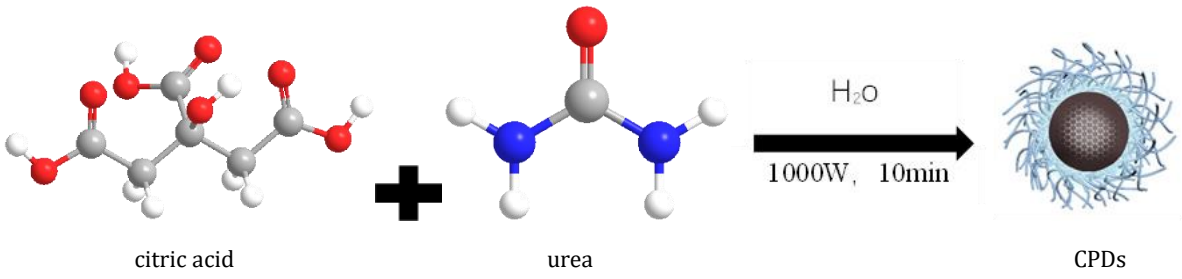

Figure 1 Synthesis of CPDs

2 Synthesis Method

As shown in Figure 1, the carbonized polymer dots were successfully synthesized by microwave method using citric acid and urea as substrates and water as solvent, and reacted for ten minutes at 1000 W. This synthesis method is low cost, easy to prepare, and the quantum yield of the reaction is high, while having good water solubility.

3 Experimental Part

3.1 Electrochemical test properties

The synthesized carbon dots were added to the 2M $ZnSO_4$ electrolyte at 3 mg / mL and stirred overnight at room temperature. The prepared electrode solution was added to the button cell for testing. Tafel and hydrogen evolution reaction tests allowed comparison of the corrosion behavior of the zinc negative electrode in the two electrolytes before and after the addition of CPDs. As shown in Figure 2 (a), the corrosion current of zinc negative electrode in $ZnSO_4$ electrolyte with CPDs added decreased from 1.156 mA cm^{-2} to 0.1257 mA cm^{-2}, which indicates that the zinc negative electrode is well protected by the addition of CPDs, and there is almost no by-products such as zinc alkali sulfate generated, which can effectively inhibit the occurrence of corrosion reaction. From the hydrogen precipitation curve in Figure 2 (b), it can be seen that the zinc negative electrode has a more negative potential response in the electrolyte containing CPDs at the same current density. It proves that CPDs contain more strongly paired functional groups with lone pair of electrons, which are able to pair with zinc ions, making the existence of free and structured water around zinc ions in the electrolyte change in form, and better inhibiting the reduction of hydrogen ions. As shown in the oxygen uptake curve in Figure 2 (c), the electrochemical stabilization window of the electrolyte with added CPDs increased from 2.52 V to 2.56 V, indicating that CPDs can be adsorbed on the electrode surface to occupy the active sites of oxygen molecules, hindering the adsorption and reduction of oxygen and inhibiting the oxygen-induced corrosion reaction. At the same time, by CA curves of zinc ion batteries under two different electrolytes, it can be concluded that the 2D to 3D diffusion transition after adding CPDs appears faster or slower, as in Figure 2 (d), the 2D to 3D transition of the $ZnSO_4$ electrolyte is in 100 s, while the 2D diffusion to 3D diffusion transition of the electrolyte with the addition of CPDs has already occurred in only 27 s, and the quicker transition it can effectively improve the ion transport efficiency and electrode kinetic performance, enhance the utilization of active sites, and alleviate the dendrite growth problem.

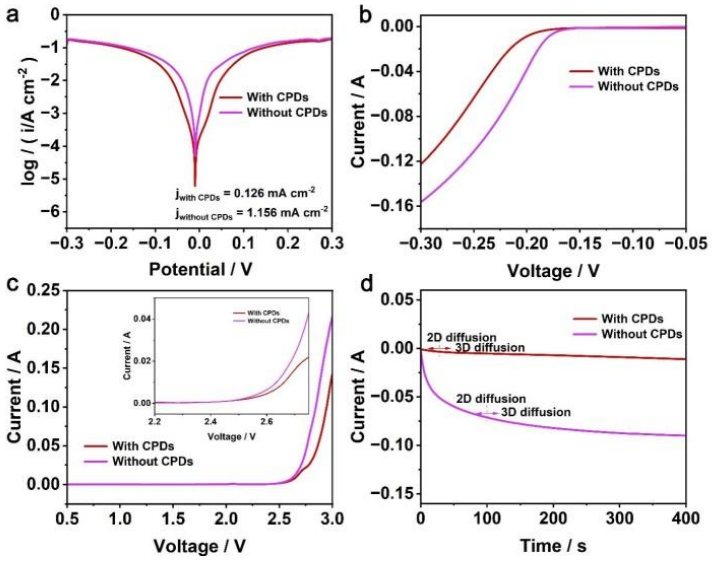

Figure 2 (a) Tafel curves. (b) HER test. (c) LSV curves. (d) Chronoamperometry (CA) curves for zinc negative electrode

Next, the electrochemical impedance (EIS) test was performed on the cell, and it can be concluded from Figure 3 (e) that the charge transfer resistance of the cell in the electrolyte containing CPDs is significantly lower than that in the $ZnSO_4$ electrolyte without CPDs, indicating that there is a fast ion transfer capability within it, so that the zinc ions and the electrons can have a fast reaction at the solid-liquid interface to alleviate the zinc deposition and improve the electrochemical performance. The values of ionic conductivity as well as ion mobility number were measured to demonstrate that the addition of CPDs has improved the ion transport kinetics of zinc ions. As shown in Figure 3 (f), the ionic conductivity of the cell was tested using electrochemical impedance test, and it was calculated that the ionic conductivity of the electrolyte with the addition of CPDs was 29.9 mS cm^{-1}, while the ionic conductivity of the electrolyte without the addition of CPDs was 24.2 mS cm^{-1}, which is a more obvious difference, indicating that the addition of CPDs effectively improves the ion transport kinetics. As shown in Figure 3 (g, h), the timed current method combined with electrochemical impedance method was utilized to indicate the transference ability of zinc ions under different electrolytes. It can be calculated that the ion mobility number in the electrolyte containing CPDs is 0.44, while the ion mobility number in the electrolyte without CPDs is only 0.17, which is because CPDs have abundant functional groups on the surface that can be combined with zinc ions, have a conductive effect to promote the transport of zinc ions, and guide the homogeneous deposition of zinc ions to inhibit the growth of branching crystals, which can effectively improve the ion transport kinetics.

3.2 Cell properties

In order to test the effect of CPDs on the electrochemical properties, we assembled Zn||Zn symmetric cells for cycle profile determination. As shown in Figure 4 (a), at a current density of 2 mA cm^{-2} and a capacity of 1 mAh cm^{-2}, the Zn||Zn symmetric cell under the $ZnSO_4$ electrolyte without CPDs completely short circuit after only 80 h of cycling, whereas the Zn||Zn symmetric cell under the electrolyte containing CPDs was able to cycle stably for more than 873 h, with a cycling life of about eleven times longer than that of the former. Moreover, as shown in Figure 4 (b) shows the enlarged cycling curves of the battery under the two electrolytes for the first 10 h. It can be seen that the polarization voltage of the battery is smaller after adding CPDs, which makes it easier for the zinc ions to nucleate uniformly, and effectively reduces the charge transfer impedance and interfacial resistance inside the battery, and promotes the rapid and uniform transmission of zinc ions. Figure 4 (c), the voltage of the former can still be kept very stable in the last 10 h of the cycle, and this gap strongly proves that the CPDs have high electrical conductivity and rich surface functional groups, which not only promote the uniform deposition of zinc ions and inhibit the growth of dendritic crystals, but also regulate the ionic flow through the distribution of the surface charge, reduce the side reactions and electrode corrosion, and effectively solve the common problems of zinc batteries, such as poor reversibility and short life.

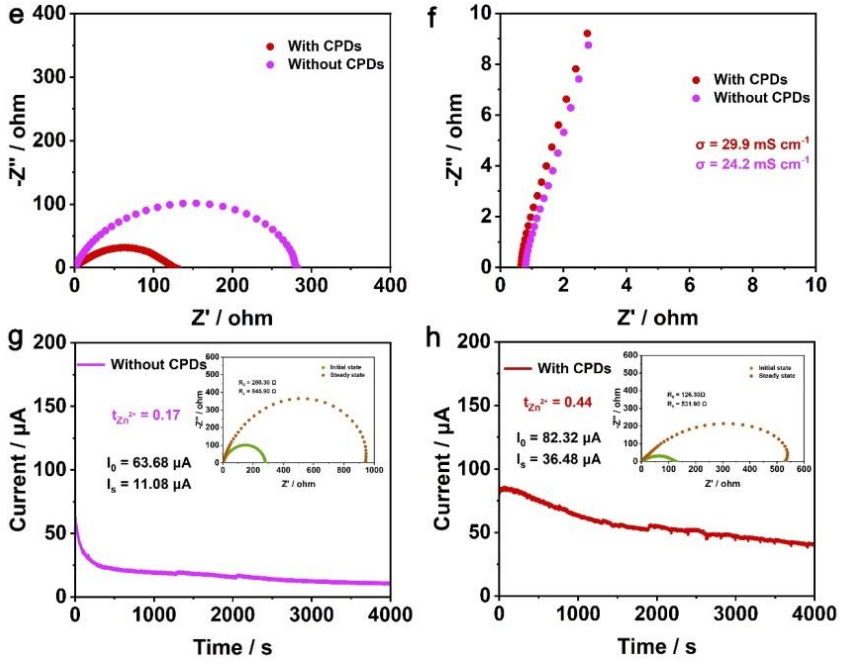

Figure 3 (e) EIS test for symmetric cell. (f) Ionic conductivity of both electrolytes. (g, h) Ionic transference number of both electrolytes

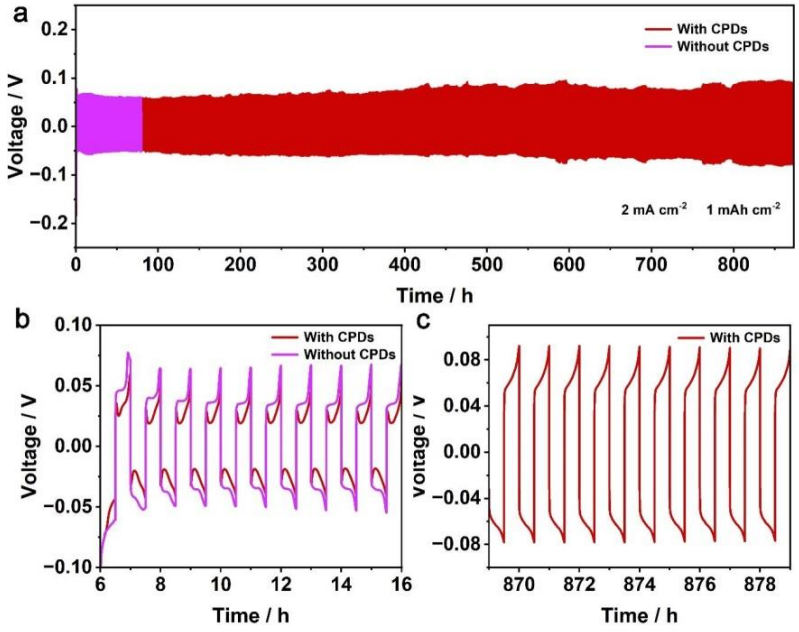

Figure 4 (a) Cycling properties of Zn||Zn symmetric cell at 2 mA cm^{-2} 1 mAh cm^{-2} current density. (b) Cycling magnification of the first 10 h. (c) Cycling magnification of the second 10 h

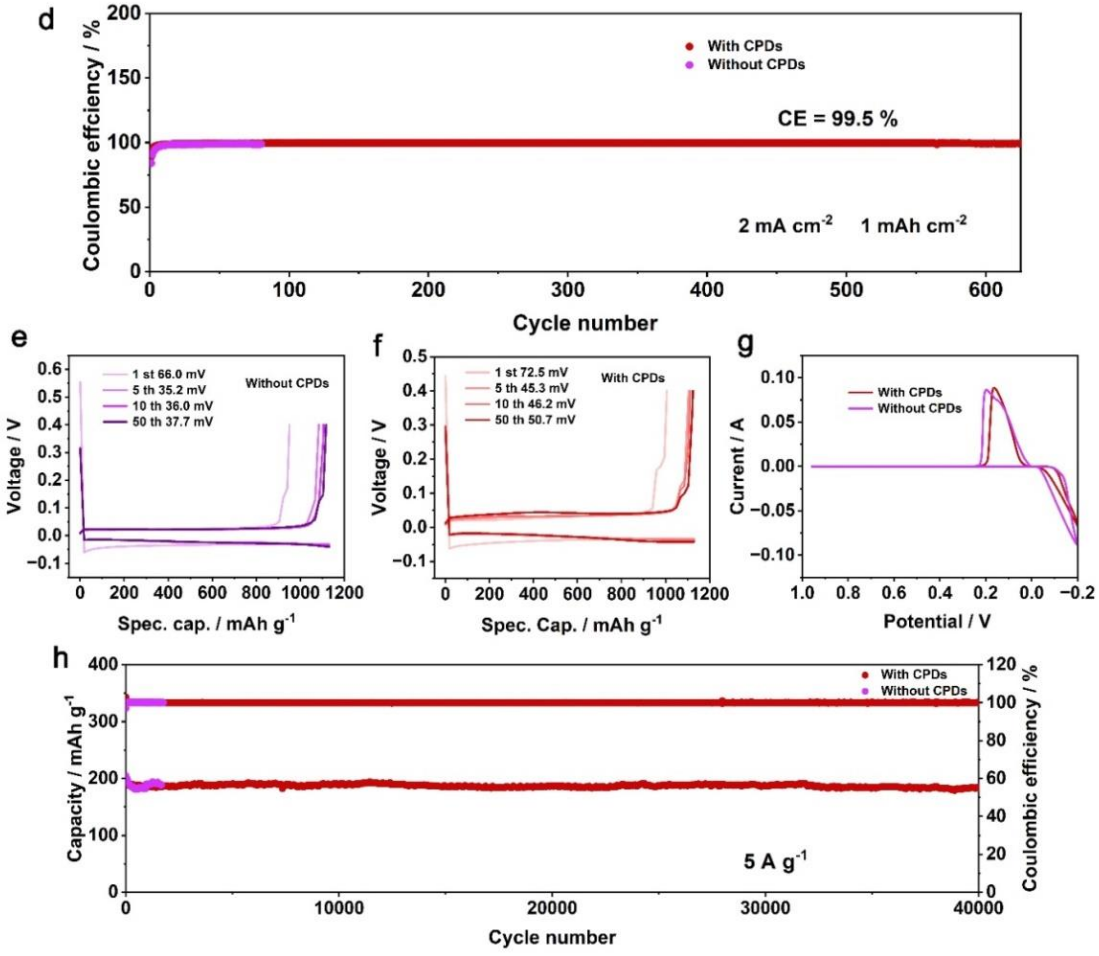

Figure 5 (d) Coulombic efficiency at 2 mA cm^{-2} 1 mAh cm^{-2} current density. (e, f) Capacity-voltage curves for different number of turns. (g) CV curves. (h) Cycling performance of the Zn || I_2 full cell at 5A g^{-1}

In addition to the stable cycling performance, CPDs as electrolyte additives can also exhibit excellent Coulombic performance in Zn||Cu asymmetric batteries. As shown in Figure 5 (d), under the condition of current density of 2 mA cm^{-2} and capacity of 1 mAh cm^{-2}, the Coulombic efficiency is unstable and the battery is short-circuited after cycling for 80 cycles in the battery with only $ZnSO_4$ electrolyte, whereas the electrolyte containing CPDs is still stable after cycling for 626 cycles and is able to reach more than 99.5%, which indicates that the CPDs are able to optimize the zinc ions' deposition/dissolution behavior, inhibit the growth of dendrites, and prevent piercing the diaphragm leading to battery short circuit.

In order to verify whether CPDs can be used as electrolyte additives for zinc ion batteries to improve the cycling performance of the batteries in practical applications. We assembled a Zn||I_2 full battery with I_2 as the cathode material. As shown in Figure 5 (h), the cell with CPDs added was able to cycle stably for about 43,000 cycles at a discharge specific capacity of about 190 mAh g^{-1} under 5 A g^{-1}, with a capacity retention of up to 90%, and the Coulombic efficiency could be maintained at 100% at all times. In contrast, the cell without CPDs electrolyte completely deteriorated after only 670 cycles, and the cycle life was drastically reduced. It is proved that the addition of CPDs can not only inhibit the dendrite growth and corrosion reaction of zinc ions, but also anchor the free iodine species by the rich oxygen/nitrogen-containing functional groups on the surface of CPDs, inhibit the shuttle effect of multiple iodides, and minimize the loss of active substances, which greatly improves the cycling stability and the Coulombic performance of the battery.

As shown in Figure 5 (e, f), the capacity voltage curves of the two electrolytes added to the cell at different number of laps, the addition of CPDs may be due to the introduction of a large number of electrolyte additives resulting in a slight increase in polarization voltage compared to the addition of the $ZnSO_4$ electrolyte, but it does not affect the cycling stability because the polarization voltage is decreasing with the increase of the number of laps. Meanwhile, as shown in Figure 5 (g) in comparing the CV curves of the two, it can also be found that the nucleation overpotential of the asymmetric cell decreases after the addition of CPDs, and the energy barrier decreases, which is conducive to the generation of zinc monomers by the reduction of zinc ions.

4 Conclusions

In summery, in order to solve the problem of zinc ion batteries hindering their development in large-scale energy storage systems due to the defects of dendrite growth, corrosion and hydrogen precipitation reaction, the electrolyte of zinc ion batteries is modified by adding carbonized polymer dots (CPDs), which are rapidly synthesized by microwave method using citric acid and urea as the substrate, as the additive of electrolyte. Through a series of electrochemical tests, cycling and coulometric performance tests, we found that CPDs have a strong adsorption capacity for Zn^{2+}, which can not only change the solvation structure of Zn^{2+}, inhibit corrosion, and reduce the occurrence of side reactions, but also improve the transport rate of Zn^{2+}, induce uniform deposition of zinc ions, and inhibit the growth of zinc ions dendritic crystals, Thus improving the properties of zinc-ion batteries. Ultimately providing a referenceable method for the development of zinc ion batteries.

Data availability: The data that support the findings of this study are available within the paper.

Acknowledgements: This work was supported by the National Natural Science Foundation of China (22035001, 22275030 and 22209023), the Jilin Provincial Education Department (JJKH20231304KJ), and the Jilin Province Science and Technology Development Plan Project (International Cooperation 20240402073GH).

References

[1] Wu Zhaofan, Luo Xiaoxiao, Shi Xiaofeng, et al. Carbon dots derived from organic drug molecules with improved therapeutic effects and new functions [J]. Nanoscale, 2025(17):4958-4973.

[2] Sui Bowen, Zhang Zhihan, Jiang Xuemei, et al. Mechanically Strong Nanocolloidal Supramolecular Plastics Assembled from Carbonized Polymer Dots with Photoactivated Room-Temperature Phosphorescence [J]. Nano Lett, 2025,25(17):7020-7028.

[3] Yang Guoduo, Wang Zhuo, Zhou Sumin, et al. Regulation of fiber surface nucleation kinetics via ordered nitrogen-rich carbon dots [J]. Chemical Engineering Journal, 2024,(492):152087.

[4] Wang Wenchen, Song Yihan, Yang Guoduo, et al. Carbonized Polymer Dots with Controllable N, O Function Groups as Electrolyte Additives to Achieve Stable Li Metal Batteries [J]. Small, 2023,19(31):2206597.

[5] Li Yanfei, Jiao Rui, Shen Xiaoyan, et al. Spherical metal mechanism toward revolution of Zn growth for ultrafast plating/stripping kinetics [J]. Energy Storage Mater, 2023(62):102934.

[6] Shen Xiaoyan, Yang Guoduo, Huang Xinyao, et al. Carbonized polymer dots as electrolyte additives for suppressing Zn dendrite growth, corrosion, and HER in Zn-ion batteries [J]. Green Chemistry, 2025,27(20):5883-5891.

[7] Qian Shangshu, Chen Hao, Zheng Mengting, et al.

Complementary combination of lithium protection strategies for robust and longevous lithium metal batteries [J]. Energy Storage Materials, 2023(57):229-248.
[8] Ruan Pengchao, Liang Shuquan, Lu Bingan, et al. Design Strategies for High-Energy-Density Aqueous Zinc Batteries [J]. Angewandte Chemie, 2022,134(17):e202200598.
[9] Shin Hong Rim, Kim Siwon, Park Junho, et al. Electrode-level strategies enabling kinetics-controlled metallic Li confinement by the heterogeneity of interfacial activity and porosity [J]. Energy Storage Materials, 2023(56):515-523.
[10] Ma Lin, Schroeder A. Marshall, Borodin Oleg, et al. Realizing high zinc reversibility in rechargeable batteries [J]. Nature Energy, 2020(5):743-749.
[11] Wang Wenhui, Li Chaowei, Liu Shizhuo, et al. Flexible Quasi-Solid-State Aqueous Zinc-Ion Batteries: Design Principles, Functionalization Strategies, and Applications [J]. Advanced Energy Materials, 2023,13(18):2300250.